

NAVAL POSTGRADUATE SCHOOL

Monterey, California



THESIS

INTEGRATED MICROWAVE AND INFRARED
PRECIPITATION ANALYSIS

by

Lisa E. Frailey

September, 1991

Thesis Advisor:

Carlyle H. Wash

Approved for public release; distribution is unlimited

T259760

REPORT DOCUMENTATION PAGE

1a. REPORT SECURITY CLASSIFICATION Unclassified			1b. RESTRICTIVE MARKINGS	
2a. SECURITY CLASSIFICATION AUTHORITY			3. DISTRIBUTION/AVAILABILITY OF REPORT Approved for public release; distribution is unlimited.	
2b. DECLASSIFICATION/DOWNGRADING SCHEDULE				
4. PERFORMING ORGANIZATION REPORT NUMBER(S)			5. MONITORING ORGANIZATION REPORT NUMBER(S)	
6a. NAME OF PERFORMING ORGANIZATION Naval Postgraduate School	6b. OFFICE SYMBOL (If applicable) 55	7a. NAME OF MONITORING ORGANIZATION Naval Postgraduate School		
6c. ADDRESS (City, State, and ZIP Code) Monterey, CA 93943-5000		7b. ADDRESS (City, State, and ZIP Code) Monterey, CA 93943-5000		
8a. NAME OF FUNDING/SPONSORING ORGANIZATION	8b. OFFICE SYMBOL (If applicable)	9. PROCUREMENT INSTRUMENT IDENTIFICATION NUMBER		
8c. ADDRESS (City, State, and ZIP Code)		10. SOURCE OF FUNDING NUMBERS		
		Program Element No.	Project No.	Task No.
				Work Unit Accession Number
11. TITLE (Include Security Classification)				
12. PERSONAL AUTHOR(S)				
13a. TYPE OF REPORT Master's Thesis	13b. TIME COVERED From To	14. DATE OF REPORT (year, month, day) 1991, September	15. PAGE COUNT 87	
16. SUPPLEMENTARY NOTATION The views expressed in this thesis are those of the author and do not reflect the official policy or position of the Department of Defense or the U.S. Government.				
17. COSATI CODES			18. SUBJECT TERMS (continue on reverse if necessary and identify by block number)	
FIELD	GROUP	SUBGROUP	Precipitation, GOES IR, SSM/I, Microwave	
19. ABSTRACT (continue on reverse if necessary and identify by block number)				
<p>GOES infrared (IR) data is intercompared with rain analyses from the SSM/I exponential rain algorithm for the purpose of determining thresholds and statistics from IR imagery which delineate oceanic rain area. Data from ERICA cyclogenesis cases were evaluated.</p> <p>Discriminant analysis was performed using IR mean cloud top temperature, standard deviation and kurtosis as discriminating variables. Resulting functions separated rain from no-rain areas with average Probability of Detection (POD) and Percentage Error (ERR) scores of 0.68 and 0.30 for development data (0.62 and 0.37 for validation data). The scheme demonstrated little skill in discriminating rain categories beyond rain/no-rain.</p> <p>An IR threshold scheme was used to delineate rain/no-rain areas by optimizing a set of evaluation statistics. Optimal thresholds attained a predetermined POD level of 0.60 while minimizing percent misclassification error and SSM/I - IR rain area difference. The scheme yielded average POD and ERR scores of 0.64 and 0.38 with IR thresholds from 229 to 232 K.</p> <p>Results for both the discriminant analysis and optimal threshold schemes compare favorably with previous studies. The use of the SSM/I rain analyses with geostationary imagery allows reliable, frequent, large scale analysis of oceanic precipitation.</p>				
20. DISTRIBUTION/AVAILABILITY OF ABSTRACT			21. ABSTRACT SECURITY CLASSIFICATION	
<input checked="" type="checkbox"/> UNCLASSIFIED/UNLIMITED <input type="checkbox"/> SAME AS REPORT <input type="checkbox"/> DTIC USERS			Unclassified	
22a. NAME OF RESPONSIBLE INDIVIDUAL Carlyle H. Wash			22b. TELEPHONE (Include Area code) (408) 646-2295	22c. OFFICE SYMBOL MR/Wx

Approved for public release; distribution is unlimited.

Integrated Microwave and Infrared Precipitation Analysis

by

Lisa E. Frailey
Lieutenant , United States Navy
B.S., Pennsylvania State University, 1982

Submitted in partial fulfillment
of the requirements for the degree of

MASTER OF SCIENCE IN METEOROLOGY AND PHYSICAL OCEANOGRAPHY

from the

NAVAL POSTGRADUATE SCHOOL

September, 1991



ABSTRACT

GOES infrared (IR) data is intercompared with rain analyses from the SSM/I exponential rain algorithm for the purpose of determining thresholds and statistics from IR imagery which delineate oceanic rain area. Data from ERICA cyclogenesis cases were evaluated.

Discriminant analysis was performed using IR mean cloud top temperature, standard deviation and kurtosis as discriminating variables. Resulting functions separated rain from no-rain areas with average Probability of Detection (POD) and Percentage Error (ERR) scores of 0.68 and 0.30 for development data (0.62 and 0.37 for validation data). The scheme demonstrated little skill in discriminating rain categories beyond rain/no-rain.

An IR threshold scheme was used to delineate rain/no-rain areas by optimizing a set of evaluation statistics. Optimal thresholds attained a predetermined POD level of 0.60 while minimizing percent misclassification error and SSM/I-IR rain area difference. The scheme yielded average POD and ERR scores of 0.64 and 0.38 with IR thresholds from 229 to 232 K.

Results for both the discriminant analysis and optimal threshold schemes compare favorably with previous studies. The use of the SSM/I rain analyses with geostationary imagery allows reliable, frequent, large scale analysis of oceanic precipitation.

TABLE OF CONTENTS

I. INTRODUCTION	1
II. SATELLITE PRECIPITATION ESTIMATION TECHNIQUES	4
A. VISUAL AND INFRARED METHODS	4
1. VIS and IR Overview	4
2. Bispectral Method	5
B. MICROWAVE	11
III. DATA	15
A. IR IMAGERY	15
B. SSM/I IMAGERY	16
C. IMAGE RECTIFICATION	17
IV. LOCALIZED RAIN/NO-RAIN STUDIES OF ERICA IOP 2 AND 4	19
A. CASE A: 13/0901 DECEMBER 1988	19
B. CASE B: 13/2301 DECEMBER 1988	25
C. CASE C: 4/2101 JANUARY 1989	30
D. OVERALL RESULTS	35

V. DISCRIMINANT ANALYSIS APPROACH	37
A. DISCRIMINANT ANALYSIS THEORY	37
B. PROCEDURE	38
C. CLASSIFICATION RESULTS	42
1. Rain / No-Rain Classification	42
2. Further Division of Rain Categories	45
VI. OPTIMAL THRESHOLD APPROACH	47
A. PROCEDURE	47
B. EVALUATION	49
C. RESULTS	50
1. Case A: 13/0901 December 1988	53
2. Case B: 13/2301 December 1988	55
3. Case C: 4/2101 January 1989	56
4. Case Comparisons	57
D. COMPARISON WITH OTHER STUDIES	59
VII. CONCLUSIONS AND RECOMMENDATIONS	62
APPENDIX A. STATISTICAL PARAMETERS	66

APPENDIX B. APPLIED OPTIMAL IR THRESHOLD	68
LIST OF REFERENCES	72
INITIAL DISTRIBUTION LIST	75

LIST OF TABLES

Table I	ERICA STORMS STUDIED	15
Table II	CASE A SAMPLE STATISTICS	23
Table III	CASE B SAMPLE STATISTICS	28
Table IV	CASE C SAMPLE STATISTICS	33
Table V	CLASSIFICATION VARIABLES. Mean values for each of the rain/no rain classification variables are indicated.	40
Table VI	LINEAR DISCRIMINANT ANALYSIS RESULTS. Results indicate percentages of categories correctly identified by the discriminant function. .	43
Table VII	RAIN INTENSITY CLASSIFICATION RESULTS. Results indicate averaged (Cases A, B and C) percentages of rain categories identified by the discriminant functions. Shaded boxes are categories correctly classified. . .	46
Table VIII	PRECIPITATION CONTINGENCY TABLE (after Lovejoy and Austin 1976)	48
Table IX	COMPARISON OF STATISTICAL RESULTS. Optimal threshold vs. average (development and validation data) discriminant analysis.	54
Table X	COMPARISON WITH VARIOUS RAIN ESTIMATION SCHEMES .	59
Table XI	PRECIPITATION CONTINGENCY TABLE (after Lovejoy and Austin 1976)	66

LIST OF FIGURES

Fig. 1	Precipitation probabilities derived from rain/no-Rain histograms. The boundary separates raining from non-raining pixels based on an optimum probability. (Lovejoy and Austin 1979)	6
Fig. 2	Decision boundaries separate clusters of VIS and IR frequency peaks. (Tsonis and Isaac 1985)	8
Fig. 3	Brightness temperatures versus rainrates for 3 microwave frequencies. (Kidder and Vonder Haar 1990)	12
Fig. 4	Case A: 13/0903 December 1988 SSM/I oceanic exponential rainrate analysis, mm/h.	20
Fig. 5	Case A: 13/0901 December 1988 GOES IR imagery. Cirrus (C) and rain (R) boxes annotated.	21
Fig. 6	Case A Distribution Histograms for analyzed cirrus and rain areas.	24
Fig. 7	As in Fig. 4, except Case B: 13/2257 December 1988.	26
Fig. 8	As in Fig. 5, except Case B: 13/2301 December 1988.	27
Fig. 9	As for Fig. 6, except Case B.	29
Fig. 10	As in Fig. 4, except Case C: 4/2147 January 1989.	31
Fig. 11	As in Fig. 5, except Case C: 4/2101 January 1989.	32
Fig. 12	As in Fig. 6, except Case C.	34

Fig. 13	Scatterplots showing distribution of Case A rain/no-rain areas as functions of a) IR mean, standard deviation and kurtosis; b) IR mean and standard deviation. "1" represents no-rain, "2" represents rain.	41
Fig. 14	Evaluation statistics POD, FAR, CSI, ERR and AREA as functions of IR value for Cases A, B, and C.	51
Fig. 15	Evaluation statistics POD, ERR and AREA as functions of IR value for Cases A, B, and C.	53
Fig. 16	GOES IR imagery for 13/0901 December 1988. Black area represents precipitation as determined by optimal IR threshold of 232 K.	68
Fig. 17	As in Fig. 16, except 13/1101 December 1988.	68
Fig. 18	As in Fig. 16, except 13/1301 December 1988.	69
Fig. 19	As in Fig. 16, except 13/1601 December 1988.	69
Fig. 20	As in Fig. 16, except 13/1901 December 1988.	70
Fig. 21	As in Fig. 16, except 13/2101 December 1988.	70
Fig. 22	As in Fig. 16, except 13/2301 December 1988.	71
Fig. 23	As in Fig. 16, except 14/0101 December 1988.	71

ACKNOWLEDGEMENT

I would like to express my sincere gratitude to my thesis advisor, Dr. Carlyle Wash, for his inspiration, support and guidance throughout this project. Many thanks are due to Dr. Philip Durkee, my second reader, for his helpful suggestions on this thesis, and to Patrick Haar for his assistance in the use and application of statistical software. I'd also like to acknowledge Kurt Nielsen and Jim Cowie for their assistance with the NPS IDEA Lab. I'm deeply indebted to Craig Motell, whose expertise in formatting and displaying satellite imagery allowed this thesis to happen.

I. INTRODUCTION

The determination of rainfall over extensive areas is important, not only for long range climatological studies, but also for real-time operational purposes. Satellite data imagery allows vast areas to be studied, areas with previously limited or non-existent observations. Of particular interest to naval operations is the determination of precipitation areas in oceanic regions.

While geostationary visual (VIS) and infrared (IR) satellite coverage of oceanic areas has been available since 1974, its use for precipitation analysis has been limited since VIS and IR data sense cloud properties, not precipitation directly. However, the recent development of precipitation algorithms utilizing satellite microwave data from the operational Special Sensor Microwave/Imager (SSM/I) yields direct oceanic precipitation information available every 12 h from current and future Defense Meteorological Satellite Program (DMSP) polar orbiting satellites.

The objective of this thesis is to intercompare IR data from the Geostationary Operational Environmental Satellite (GOES) with DMSP SSM/I precipitation analyses. The intercomparison should allow the determination of IR thresholds and statistics which delineate the rain area. These thresholds can be used for subsequent hourly rain analyses until microwave verification data is again available, six or 12 h later. GOES and SSM/I data are currently used by the Navy, and a precipitation delineation scheme utilizing these data types could readily be incorporated into an operational product.

IR and microwave data from the Experiment on Rapidly Intensifying Cyclones over the Atlantic (ERICA) will be used in this thesis. ERICA was conducted from 01 December 1988 to 28 February 1989 over the northwest North Atlantic Ocean. Centering on the climatologically favored area for rapid cyclogenesis, it spanned an area from 30N to 50N, 80W to 50W. The objectives of ERICA (Hadlock and Kreitzberg 1988) were to: (1) understand the fundamental physical processes occurring in the atmosphere during rapid intensification of cyclones at sea, (2) determine those physical processes that need to be incorporated into dynamical prediction models through efficient parameterizations, and (3) identify measurable precursors that must be incorporated into the initial analysis for accurate and detailed operational model predictions. ERICA data includes eight Intensive Observational Periods (IOP's) of 36 to 48 h duration. Each IOP covers the development of a rapid cyclogenesis event, defined as an extratropical surface cyclone whose central pressure fall averages at least one mb/h for 24 h. ERICA measurements were made from aircraft, buoys, satellites, soundings and radar. This variety of data makes ERICA storms an ideal test bed for oceanic precipitation analysis.

Specific objectives of this thesis are:

1. Investigate differences in IR brightness temperature (T_b) values between SSM/I-determined raining and other non-raining clouds such as dense cirrus.
2. By optimizing selected statistical parameters, determine an IR T_b threshold which delineates precipitation as determined by SSM/I data.

A literature review of precipitation analysis methods using various combinations of VIS, IR , radar and microwave data is presented in Chapter II. Chapter III details how the ERICA IR and SSM/I data used in this analysis was obtained and prepared. The initial analysis of localized areas within the ERICA storms is presented in Chapter IV, followed by a discriminant analysis approach to precipitation delineation in Chapter V. Chapter VI explores an IR thresholding scheme for precipitation analysis. A summary with conclusions and recommendations for future research and implementation of these schemes is presented in Chapter VII.

II. SATELLITE PRECIPITATION ESTIMATION TECHNIQUES

A. VISUAL AND INFRARED METHODS

1. VIS and IR Overview

The estimation of rain with VIS and IR data is subjective, as precipitation is not sensed directly. Rather, VIS and IR yield information about cloud thickness and cloud top temperature, respectively. Cloud type is inferred from these values, and rain area and rate further inferred from the cloud type. Four basic methods are currently used to delineate rain areas with VIS and IR (Barrett and Martin 1981):

1. Cloud Indexing
2. Cloud Life History
3. Cloud Model
4. Bispectral

Cloud Indexing is the oldest method, and it is based on identifying the cloud types. A standardized rain rate is then applied to each cloud type. With Cloud Life History, rain rate is a function of the stage in the cloud's life cycle. Griffith et al. (1978) derived a diagnostic method to estimate rainfall using this method. Stout et al. (1979) also employed the Cloud Life History method. They examined the relationship between radar-estimated rain rate and satellite-measured cloud area, focusing on the concept that precipitation peaks while the cloud area is rapidly growing. The Life History method

is a valuable research tool, but is not adequate for real-time application as it requires tracking a cloud through its development before assigning a rain rate. Cloud Models are being developed which incorporate cloud physics knowledge into the retrieval process. These can use combinations of the other three methods, but are currently in developmental stages and not available for operational use.

2. Bispectral Method

Bispectral methods intercompare VIS and IR data, where high VIS values indicate thick, bright clouds and high IR values indicate cold cloud top temperatures (Kidder and Vonder Haar, 1991). The first application of a bispectral method was conducted by Reynolds and Vonder Haar (1976), where cloud heights and amounts were determined using simultaneous VIS and IR satellite data. On a two axis (VIS and IR) plot, stratus clouds appear as bright and warm, while convective rain clouds are clustered in the cold, bright region. Threshold values for both axes can be determined to differentiate cloud types. Bispectral methods, because of their ease and consistently good results, are quite suitable for real-time operational use.

A bivariate frequency distribution to differentiate raining/non-raining clouds was developed by Lovejoy and Austin (1979a). Their use of radar observations to train a technique to recognize precipitation clouds is termed the RAINSAT approach. Pixels were assigned to either "Rain" or "No Rain" VIS/IR histograms, based on Canadian ground and shipboard radar data. The plots were combined to yield a bispectral (VIS/IR) frequency plot of precipitation probabilities (rain pixels/total pixels) for each VIS/IR

geographical areas were then constructed by applying the VIS and IR values specified by the optimal boundary and minimizing a misclassification error function. The authors found that while VIS data gave more information than IR, IR data was useful in convective cloud studies. A bispectral method was determined more accurate than a single channel method. Another finding was that actual rain area was approximately 1/4 the size of the cloud cover.

Lovejoy and Austin (1979b) investigated the sources of error in bispectral rain estimation, determining the amount of error due to errors in rain area determination versus error in rain rate algorithms. From the magnitudes of error found, they concluded that current VIS and IR schemes were good for determining rain areas, but not rain rates.

Tsonis and Isaac (1985) used a two part method to determine rain area from VIS and IR satellite data. The first part was to differentiate raining from non-raining clouds using a cluster analysis. Results of a bivariate frequency distribution were plotted on a scatter diagram, and divided into three clusters. Cluster 1 consists of points associated with clear skies and nonraining clouds, while Cluster 2 consists of points corresponding to nonraining low-level overcast, fog and haze. Cluster 3 consists of points assigned mainly to raining clouds, but includes some cirrus. Decision boundaries to separate the clusters were drawn by intersecting a point equidistant from the three cluster centers. Results are illustrated in Figure 2.

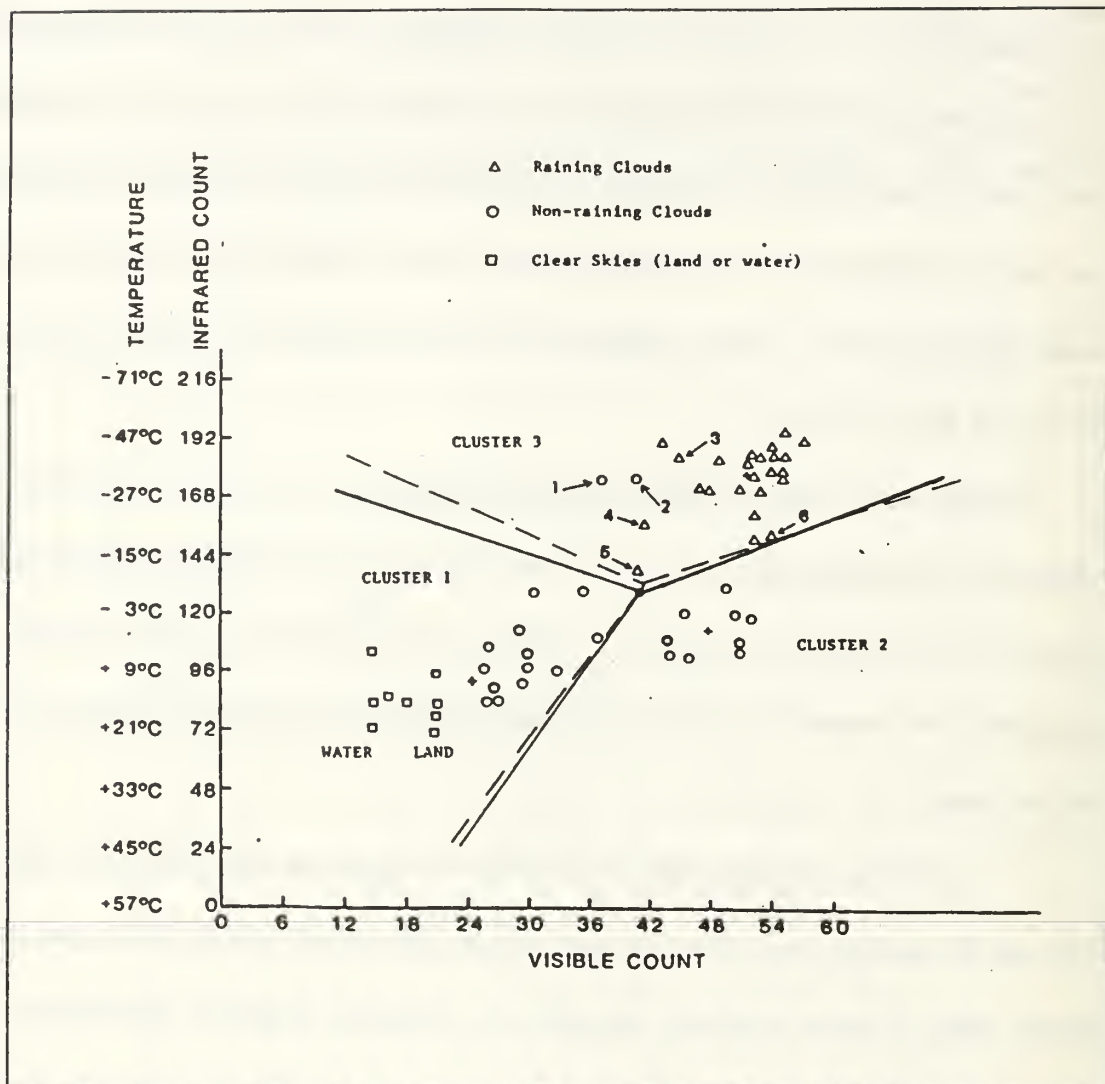


Fig. 2 Decision boundaries separate clusters of VIS and IR frequency peaks. (Tsonis and Isaac 1985)

The second part of Tsonis and Isaac's method was to determine a specific VIS threshold which would delineate the rain area from Cluster 3. Using land-based radar as ground truth, a VIS threshold was established which gave a satellite/radar rain area near unity. The authors outlined two evaluation parameters:

1. Probability of Detection: $POD = (\text{satellite correctly classified rain area}) / (\text{radar rain area})$
2. False Alarm Ratio: $FAR = (\text{satellite incorrectly classified rain area}) / (\text{satellite rain area})$

Their VIS threshold yielded a POD of 0.66 and an FAR of 0.37. Tsonis and Isaac concluded that while most of the rain area information was derived from VIS data, for cases of strong convection, a single IR threshold could accurately delineate rain area. The authors' method gave best results for convective, versus stratiform, cases.

Tsonis (1988) evaluated a simpler rain area delineation approach which used a single VIS or IR threshold. Compared to more complicated schemes, this single threshold approach performed quite adequately. Optimal thresholds yielded POD and FAR scores of 0.62 and 0.38 (VIS threshold) and 0.60 and 0.40 (IR threshold). Tsonis concludes that the simplicity and accuracy yielded by a single threshold technique may make it useful for delineating precipitation area on large scales.

Negri and Adler (1987a) used a "Grid Cell" approach to estimate rain from VIS and IR data. Focusing on subtropical convective systems, their approach explored the relationship between cloudy grid cells (determined by VIS/IR threshold values) and the variability of the precipitation within. Unlike the methods of Lovejoy and Austin or Tsonis and Isaac, IR, versus VIS, parameters were used to explain most of the variability. The authors found that while high rainrates required low cloud top temperatures, these low cloud top temperatures did not necessarily yield high rainrates.

The authors concluded that that on the scales used, useful and accurate estimates beyond rain/no-rain discrimination were unlikely.

Negri and Adler (1987b) describes a "Cloud Definition" approach to precipitation delineation, where cloud area was defined by an IR threshold. The authors sought to maximize a Critical Success Index (CSI), incorporating POD and FAR (Appendix A). They found a good correlation between IR-determined cloud area and rain area, but limited usefulness of VIS data.

Results of the "Grid Cell" and "Cloud Definition" approaches were used to formulate the Convective-Stratiform Technique (CST) by Adler and Negri (1988). This method defines convective cores by their IR temperature minima and strong temperature gradient. Rainrate and rain area are assigned to the cores as a function of IR cloud top temperature. A stratiform rain algorithm, based on the mode temperature of thunderstorm anvils, completes the convective/stratiform rain estimation.

While Negri and Adler focused on IR values to determine precipitation in the subtropics, King (1990) evaluated the relative importance of VIS and IR data in determining midlatitude rainrates. Using the Lovejoy and Austin (1979a) RAINSAT approach, King compared VIS and IR GOES data with coincident radar rainrate data. He concluded that both rainrate and fractional rain volume showed a stronger relationship with VIS count than with IR count. King's results enabled the construction of probability of rain and rainrate contours based on bispectral VIS and IR data.

Further expanding on the bispectral concept, Neu (1990) evaluated an automated multispectral (AVHRR VIS, IR, and IR split-window) nephanalysis model, with the goal of cloud type classification on a multispectral axis. He verified the automated results with a subjective cloud analysis consensus, and was able to successfully distinguish 11 cloud types. His strongest results were in determining precipitation clouds, showing that multispectral analysis could yield fast, accurate results in cloud type determination.

These studies show that precipitation areas can be delineated using VIS and/or IR satellite data. Such data is readily available from geostationary satellites, yielding continuous, real-time coverage of extensive global areas. The methods described generally utilized surface-based radar as ground truth, and focused on areas close to land.

B. MICROWAVE

Like radar, microwave remote sensing is a method of directly sensing precipitation, either through absorption/emission or scattering of radiation by precipitation. Unlike the surface-based radar used in the previous studies, however, satellite-based microwave sensors give global coverage from a platform similar to satellite VIS and IR sensors.

Figure 3 depicts the nonlinear relationship of brightness temperature (T_B) to rainrate over ocean and land backgrounds for three microwave frequencies (Kidder and Vonder Haar 1990). T_B - rainrate relationships have been used by several authors, including Wilheit and Chang (1980) and Spencer et al. (1989), to estimate rainrate.

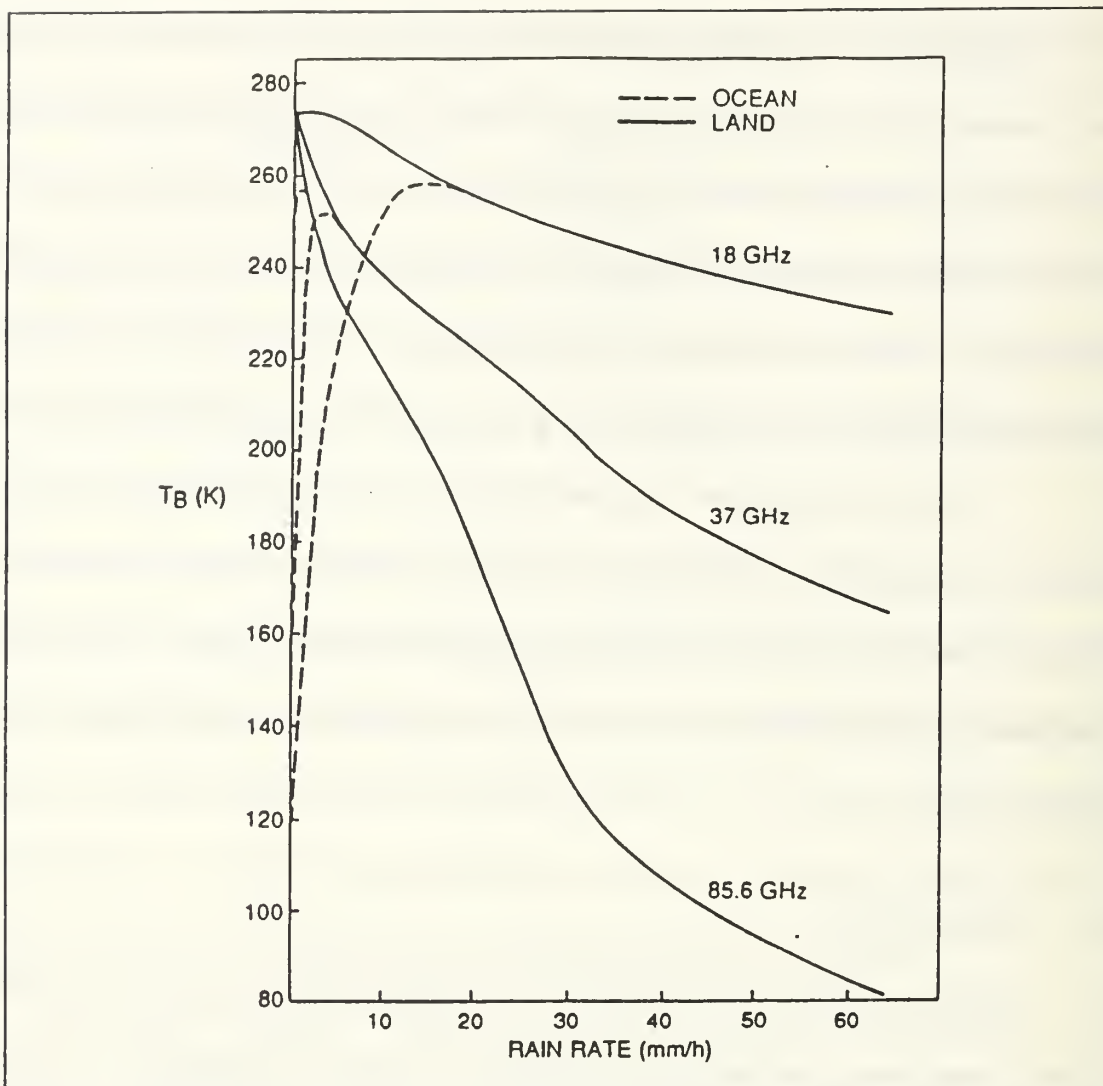


Fig. 3 Brightness temperatures versus rainrates for 3 microwave frequencies. (Kidder and Vonder Haar 1990)

Cataldo (1990) evaluated several microwave rain algorithms, determining that the initial SSM/I Hughes Aircraft Company (HAC) algorithm was inadequate for determining rain rates. He found that using T_B from the horizontally polarized 37 GHz channel (37H) yielded the best rainrate results. 37H uses an absorption regime, is sensitive to low rainrates and has little noise interference. For the 37H channel, Cataldo,

used a threshold temperature of 190 K as a rain/no-rain cutoff, with increasingly warmer temperatures to 255 K for heavier rainrates. Using coastal radar and ship reports as ground truth, he concluded that satellite-based microwave data could successfully delineate oceanic rain areas, and could further define rainrates.

Almario (1991) examined a more recently developed exponential rain algorithm which incorporates data from multiple SSM/I channels (Olson et al., 1991). Comparing the SSM/I results with aircraft and ground-based radar observations for several ERICA storms, Almario found that the exponential algorithm produced successful results in detecting oceanic rain/no rain areas and rain intensity. Results using the exponential algorithm were found to be far superior to those found using either the HAC algorithm or 37H channel. Comparisons with GOES IR imagery revealed that most of the cold cloud top (heavy convection) regions coincided with maximum rainrates in the SSM/I analyses.

There are several potential error sources inherent in microwave rainfall determination. First, microwave resolution is poor. The resolution for the 37 GHz channel is 32 km - significantly less than for VIS and IR channels. The large footprint characteristic of microwave radiometers introduces a problem with beam-filling and nonlinearity. The radiometer averages the T_b over this large footprint. However, this average does not necessarily yield a representative mean rainrate because of the nonlinearity of T_b in rainrate. This beam-filling problem generally results in an underestimation of the mean rainrate within the footprint.

Notable success has been obtained using improved microwave rain algorithms to delineate rain areas and rainrates. With microwave data, accurate rain analyses can be attained at 12 h intervals over large land and ocean areas. Thus far, surface radar has been used as ground truth for the development of VIS and IR precipitation analysis schemes. With coverage far exceeding that of surface radar, SSM/I rain analyses are logical candidates to use as ground truth for oceanic studies. This utilization should significantly improve precipitation analysis over oceanic areas, where conventional verification data is notably sparse.

III. DATA

The choice of data to be analyzed was based primarily on the availability of coincident digital GOES IR and DMSP SSM/I images which covered well-developed ERICA storms. Because of the time of day and consequent sun angle, there was no adequate GOES VIS imagery for the time periods examined. Table I summarizes the data sets used in this analysis, referred to as Cases A, B, and C; all times are Universal Coordinate Time. Synoptic descriptions of each case follow in Chapter IV.

Table I ERICA STORMS STUDIED

Case	IOP	Date	Time of Image (UTC)	
			GOES	SSM/I
A	2	13 Dec 88	0901	0903
B	2	13 Dec 88	2301	2257
C	4	4 Jan 89	2101	2147

A. IR IMAGERY

IR (10.5-12.5 μm) imagery is obtained from the Visible and Infrared Spin Scan Radiometer (VISSR) flown aboard the GOES-East satellite. The spatial resolution for each pixel at nadir is 8 x 4 km (8 km resolution north-south and 4 km east-west), where the 4 km resolution is obtained by oversampling in the east-west direction. IR imagery

is displayed on the NPS IDEA Lab as 512 x 512 pixel images. The intensity range of the IR pixels is 0 - 255 counts. Values of IR count are easily converted to equivalent brightness temperatures (T_B) using a standard IR calibration table (Ensor 1978).

B. SSM/I IMAGERY

SSM/I data are obtained from the polar orbiting DMSP satellite. Vertically and horizontally polarized 19, 35 and 85 GHz data channels are available on the SSM/I sensor, along with a vertically polarized 22 GHz channel. Resolution is proportional to the channel's frequency, and ranges from 13 km for the 85 GHz channel to 50 km for the 19 GHz channel. Brightness temperatures from these seven channels (referred to as 19V, 19H, 22V, 37V, 37H, 85V and 85H) are incorporated into the exponential rain rate algorithm and screening logic developed by Olson et al. (1991). The algorithm used is specific for oceanic rainfall, and its accuracy when applied to ERICA storms was explored and verified by Almario (1991). Both Olson (1991) and Almario (1991) found that the rainrates derived from the SSM/I exponential algorithm corresponded well with radar-derived rainrates, and were superior to rainrates derived from previous algorithms. However, validation of the exponential algorithm has thus far been qualitative, and no accuracy figures have yet been established. The results of the exponential algorithm are displayed in a 512 x 512 pixel image as rainrates from 0 to 25 mm/h. Because of the multichannel incorporation, resolution of the image is reduced to the coarsest of the seven channels, 50 km.

C. IMAGE RECTIFICATION

IR and SSM/I images were originally displayed in their natural coordinate systems for processing convenience. However, in order to compare the two image types, they must be displayed using the same projection. Image rectification, also known as "real world image mapping," is a solution to this problem (Bernstein, 1983). IR and SSM/I images for each case were rectified to a common Cylindrical Equidistant (CED) projection. Images were navigated, and latitudes/longitudes were specified so that the IR image covered the same geographic area as the corresponding SSM/I image. Images could then be intercompared, pixel by pixel. A landmasking routine was also applied to enable easy discrimination between land and ocean areas when searching the data pixels.

The area represented by each rectified pixel is dependent on the size of the geographic area specified. For Cases A and B, each pixel represents approximately 4.5 x 4.5 km, while Case C pixels cover about 6 x 6 km. Actual image resolution, however, is unchanged from the original data, and remains at 8 x 4 km for IR and 50 x 50 km for SSM/I images. Because of the discrete sampling performed in the image rectification process, gaps can occur when high resolution (IR) images are remapped. These gaps are filled using a pixel interpolation method. For low resolution images (SSM/I), only one image pixel is used for each screen pixel, and no interpolation is required.

Rectified IR and SSM/I images constitute the data base for the analyses to be performed in this study. Navigation and remapping to equivalent projection allows pixel by pixel intercomparison for the precipitation analyses described in the following chapters.

IV. LOCALIZED RAIN/NO-RAIN STUDIES OF ERICA IOP 2 AND 4

Selected areas of cold GOES IR temperature, determined by SSM/I analysis to be either raining or nonraining, were examined to determine if any information existed within the IR data that could successfully discriminate rain from no-rain/cirrus for Cases A, B, and C (Table 1).

The SSM/I exponential rainrate algorithm was applied to each case, yielding a display of rain area and rainrates. This display was used as ground truth in choosing 20 x 20 pixel areas, (referred to as "cloud boxes") from the GOES IR imagery. The cloud boxes were positioned so that the rainrates within each box were as homogeneous as possible. A representative collection of no rain (cirrus), light (1-2 mm/h), moderate (2-4 mm/h), and heavy (>4 mm/h) rain areas was selected. GRAFSTAT statistical analysis software (Burkland et al. 1990) was used to evaluate the 20 x 20 pixel IR data arrays. A histogram and set of sample statistics were generated for each cloud box to investigate cloud top temperature differences between the rain and no-rain areas.

A. CASE A: 13/0901 DECEMBER 1988

Case A GOES and SSM/I imagery (Figures 4 and 5) describes the first of two storm systems during IOP 2. The first upper-air trough moved offshore of the Georgia - South Carolina coast shortly after 13/0000. A surface cyclone developed with this system, deepened modestly for the initial 12 h period and moved eastward along 30N.

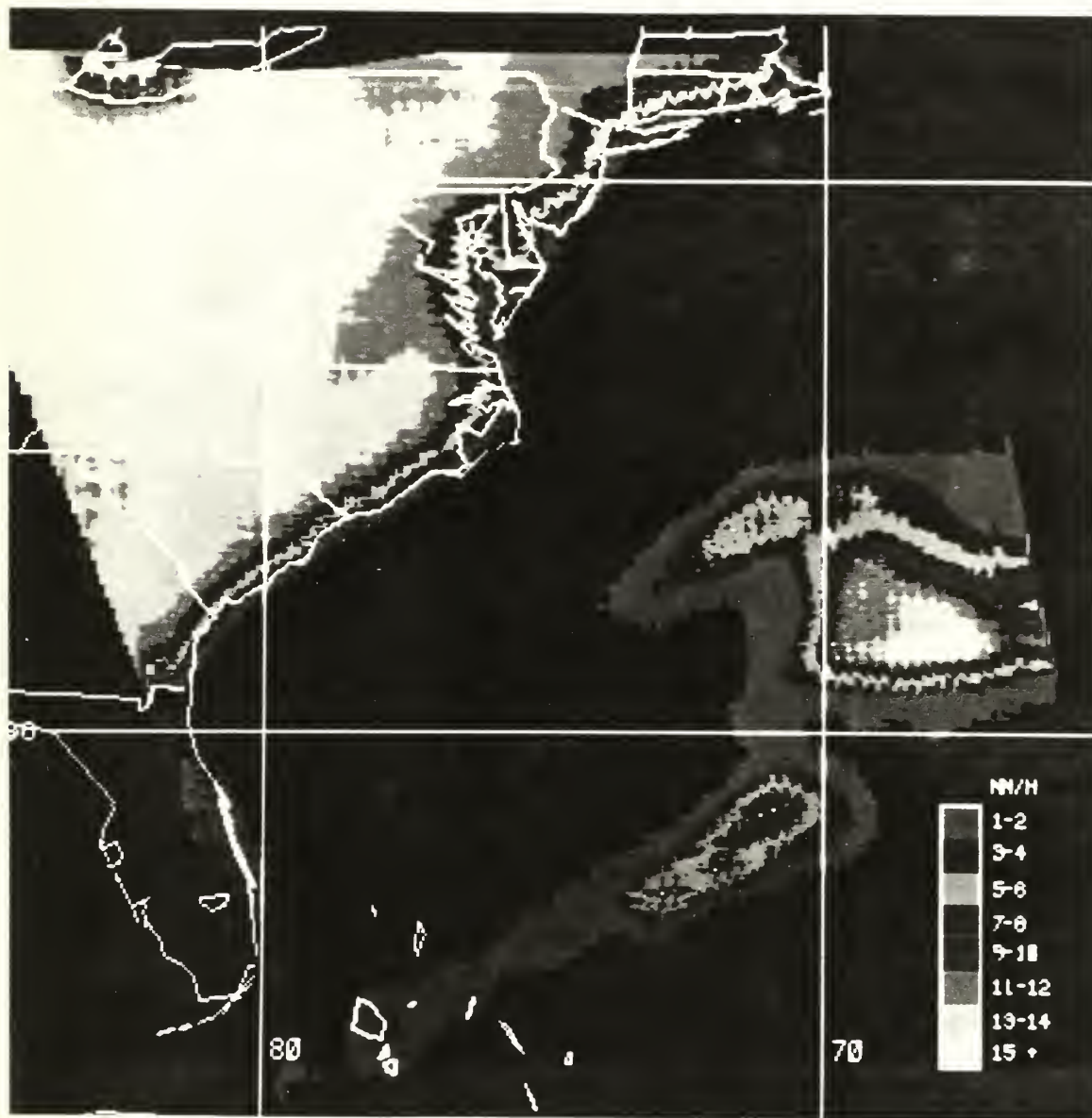


Fig. 4 Case A: 13/0903 December 1988 SSM/I oceanic exponential rainrate analysis, mm/h.

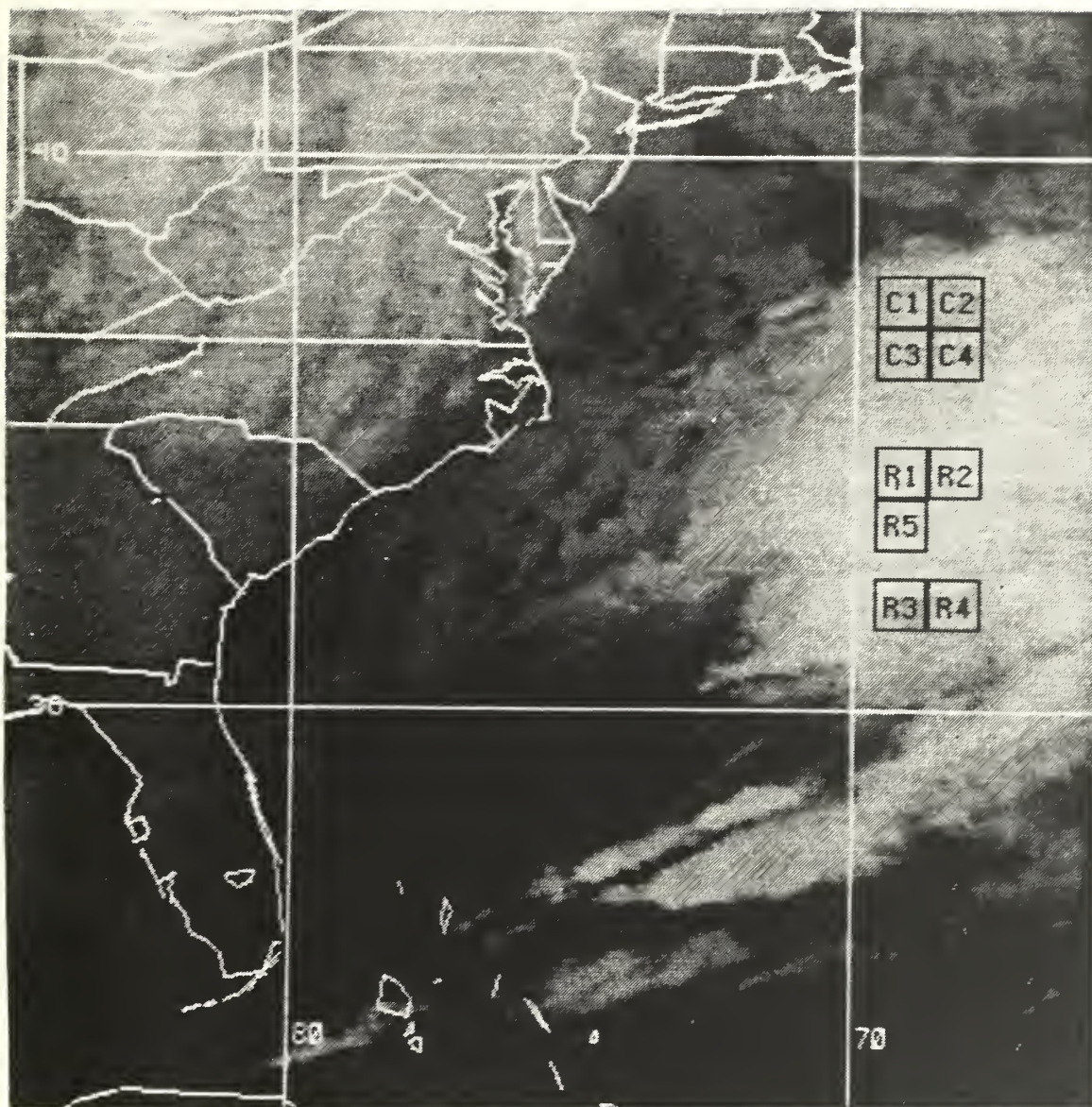


Fig. 5 Case A: 13/0901 December 1988 GOES IR imagery. Cirrus (C) and rain (R) boxes annotated.

By the time of this SSM/I pass, the cyclone had developed into a comma-shaped cloud. Its 1004 mb storm center is centered near 33N 68W. (Hartnett et al. 1989)

The SSM/I exponential rain algorithm analysis results are given by Figure 4, with rainrates coded by mm/h. Heaviest precipitation (15 mm/h) lies east of the cyclone center, and is surrounded by relatively concentric areas of decreasing rainrate. A band of moderate and heavy rainfall extends east of the system center associated with the warm front, while a second band (cold front) extends southwest to the Bahama Islands. Figure 5 presents the concurrent GOES IR imagery. While the GOES IR overall cloud area and shape coincide with the SSM/I-determined rain area, cirrus is evident north of the primary rain area. The cloud boxes analyzed are indicated, and labeled as "C" (cirrus) or "R" (rain). The locations of the boxes were chosen to study cloud top temperatures between the cirrus area and the raining area to the south.

An analysis of the resulting sample statistics (Table II) and distribution histograms (Figure 6) for the cloud boxes reveals clear differences between the rain and no-rain samples. The no-rain (cirrus) samples resemble each other closely, both in their distribution shape and in the IR mean (185.39) (232.5 K) and standard deviation (2.97). The rain samples are characterized by a higher mean IR count (197.71), colder cloud top temperature (220.8 K) and generally lower standard deviation. Rain samples, however, are not homogeneous, but appear to vary according to rainrate. Samples R1 and R2 represent light and moderate rainrates, and exhibit high mean (203.17) (214.8 K) and low standard deviation (1.07) values. These are in sharp contrast with the lower mean

Table II CASE A SAMPLE STATISTICS

Box	Rainrate	Mean	Std.Dev.	Kurtosis
C1	0	185.43	2.35	2.38
C2	0	183.15	3.54	4.42
C3	0	184.61	1.75	2.90
C4	0	188.37	4.22	5.12
Mean C		185.39	2.97	3.71
R1	Lt/Mod	203.34	1.12	3.08
R2	Lt	203.01	1.02	4.91
R3	Hvy	188.00	12.18	2.06
R4	Hvy	192.27	4.34	2.15
R5	Hvy	201.92	1.17	3.86
Mean R		197.71	3.97	3.21

(194.06) (223.9 K) and higher standard deviation (5.89) values corresponding to the high rainrate samples R3, R4 and R5.

Analysis of color-enhanced IR cloud top temperatures (not shown) reveals that cloud boxes with light and moderate rainrates (R1 and R2) coincide with areas of uniform cloud top temperatures, as suggested by the low standard deviation values. While R5 is categorized as heavy rain, the SSM/I imagery shows that the area contains several rainrate levels ranging from 5 to 11 mm/h, and appears to be a transition area from moderate to heavy convective rain areas. This may explain why the statistics for R5 more closely resemble those of the light/moderate rain boxes than of the heaviest rain boxes. Cloud boxes R4 and R5 are represented in the enhanced GOES imagery as areas of significant cloud top temperature variability, with strong cloud top temperature

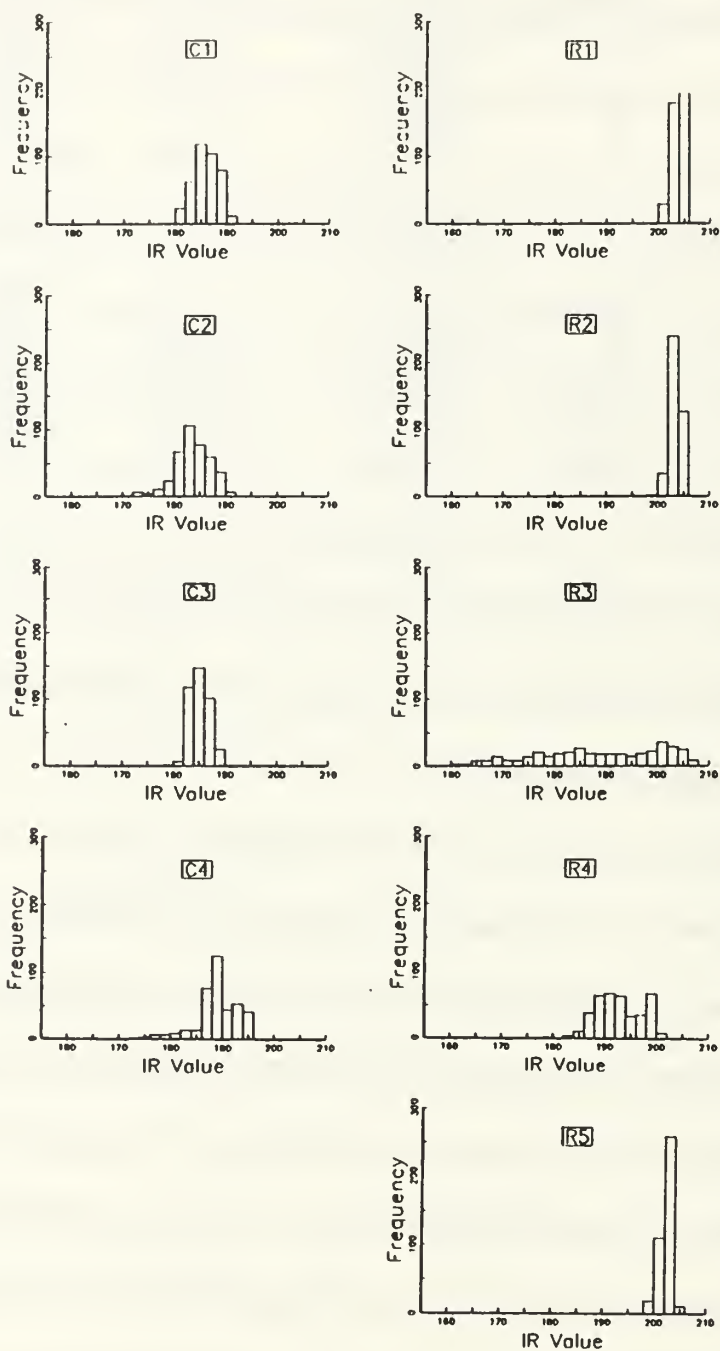


Fig. 6 Case A Distribution Histograms for analyzed cirrus and rain areas.

gradients. Such a cloud top temperature pattern is consistent with the towering cumulus (and compensating descent areas) associated with heavy convective rain. Kurtosis values were evaluated, but appear to have no discernible pattern in differentiating rain/no-rain areas.

It is apparent from the analysis that mean IR count and standard deviation can be used to differentiate rain from no-rain areas for this case. Notable points are the Gaussian distribution of cirrus IR values and the variations of rain IR values with rainrate.

B. CASE B: 13/2301 DECEMBER 1988

Case B satellite imagery (Figures 7 and 8) depict the second storm system in IOP 2. This second, stronger upper-air trough with associated upper-level jet streak moved offshore from Virginia and North Carolina at about 13/1200. A surface trough developed northward from the Gulf Stream off Cape Hatteras towards Long Island and southern New England. Central pressure of the system at 13/2300 was approximately 995 mb, with rapid intensification to occur during the next 12 h. (Hartnett et al. 1989)

Cirrus and rain cloud boxes were chosen on the basis of concurrent SSM/I precipitation analysis (Figure 7), and are labeled on the GOES IR imagery (Figure 8). While SSM/I rain area is within the confines of the GOES high cloud area, extensive cirrus cover is apparent both east and north of the system center, probably blown off from the storm center by the upper-level jet. Again, cloud boxes were chosen to study cloud top temperature differences between the downstream cirrus and rain areas.

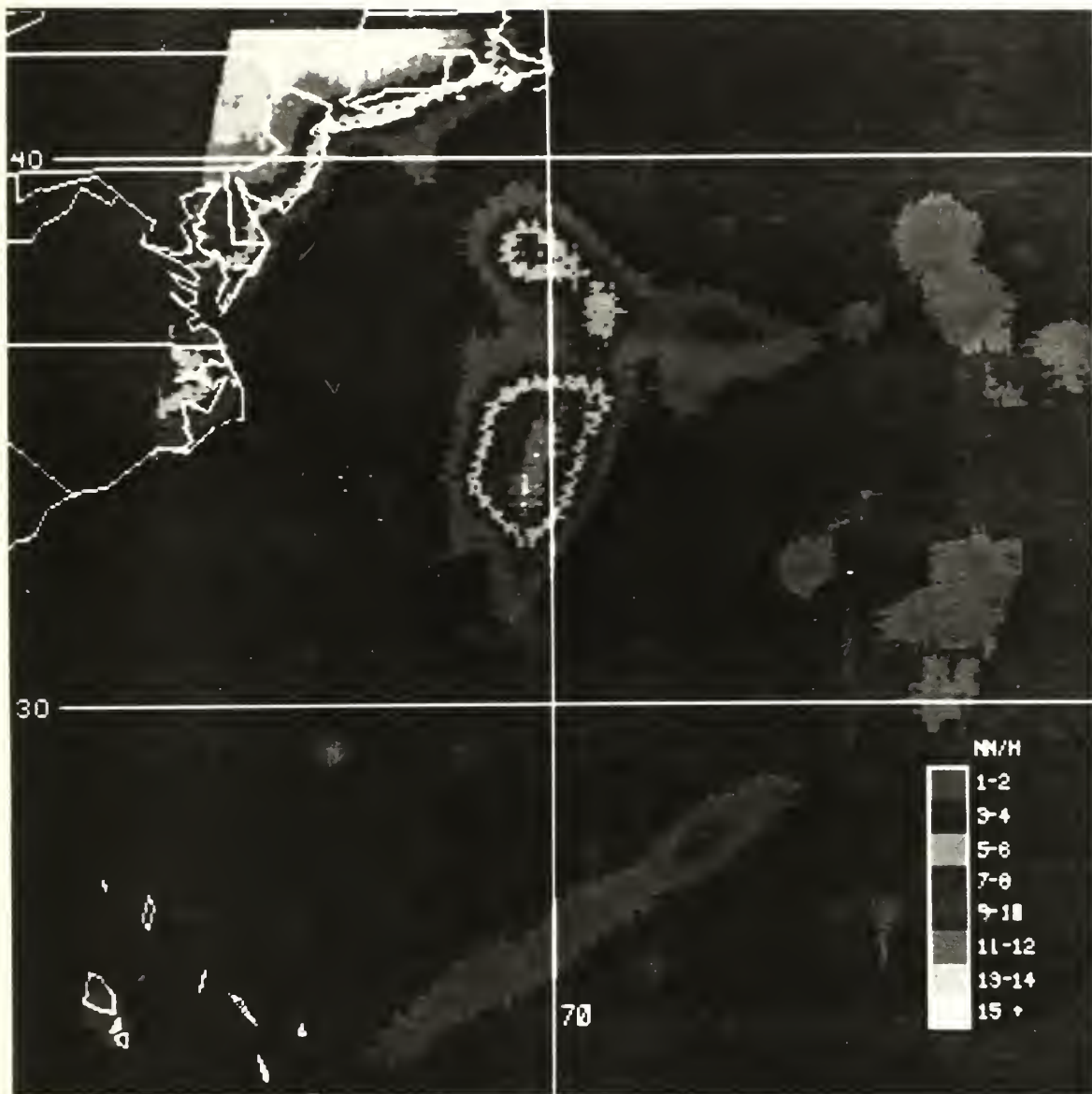


Fig. 7 As in Fig. 4, except Case B: 13/2257 December 1988.

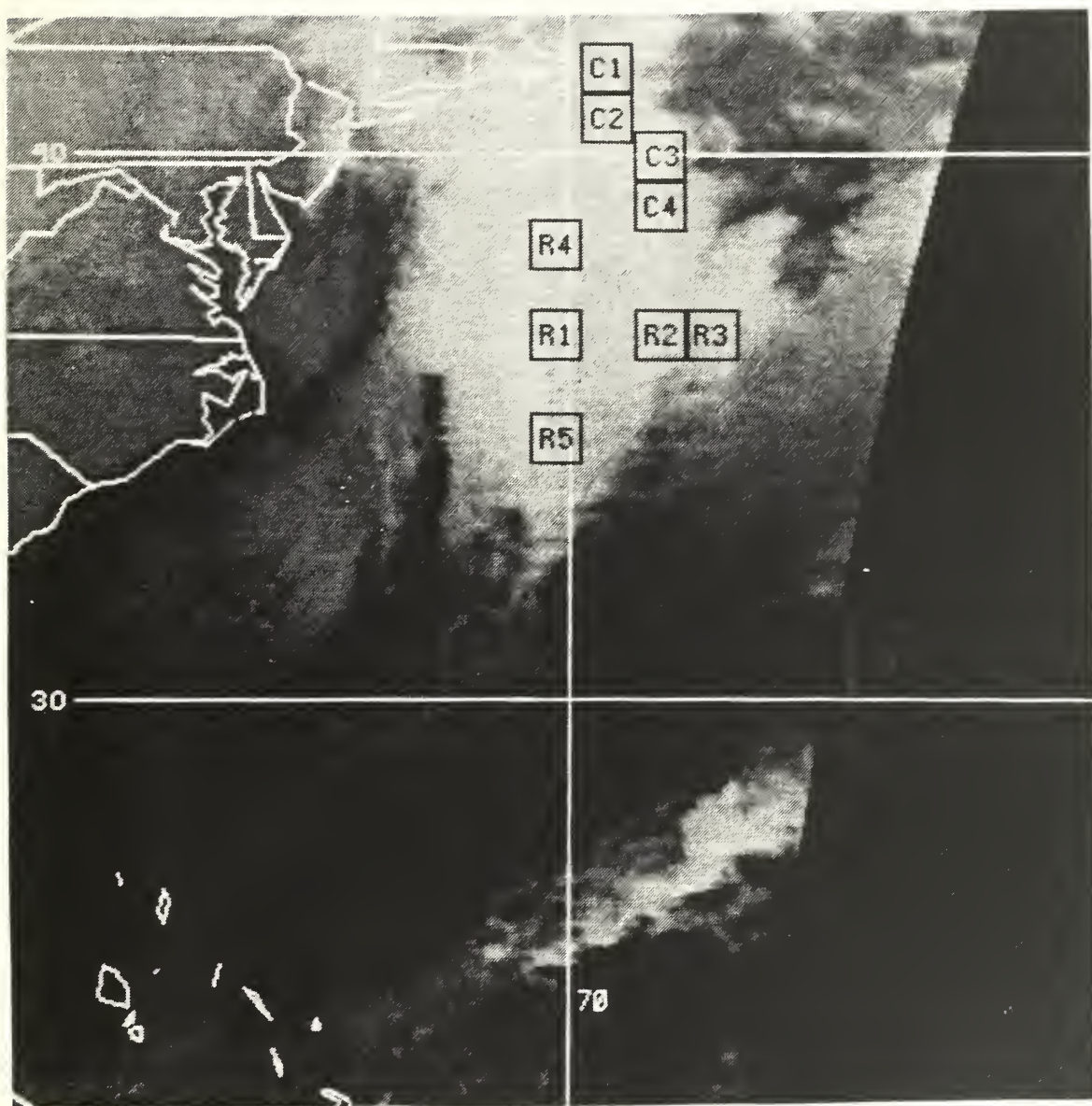


Fig. 8 As in Fig. 5, except Case B: 13/2301 December 1988.

The heaviest rain area (11-13 mm/h) is centered at 37N 71W. Also seen on this imagery is a trailing frontal band from the storm system analyzed in Case A.

Table III CASE B SAMPLE STATISTICS

Box	Rainrate	Mean	Std.Dev.	Kurtosis
C1	0	188.54	3.34	3.43
C2	0	194.65	1.84	3.52
C3	0	191.76	6.58	10.06
C4	0	191.50	2.53	2.74
Mean C		191.61	3.57	4.93
R1	Lt	196.10	0.88	2.48
R2	Lt	186.64	5.41	3.31
R3	Lt/Mod	182.34	3.73	3.06
R4	Hvy	195.43	2.02	2.35
R5	Hvy	186.15	3.51	2.01
Mean R		189.33	3.11	2.64

Sample statistics for Case B are presented by Table III and distribution histograms by Figure 9. In contrast to the results in Case A, no large temperature differences are apparent between the cirrus and rain boxes for this case. In fact, the mean for cirrus cloud boxes is slightly colder (191.61) (226.4 K) than the mean for rain boxes (189.33) (228.7 K). The imagery constraints allowed only analysis of cirrus boxes from the northeastern quadrant of Case B's cyclone system, whereas cirrus boxes from the northwest quadrant of Case A's system were analyzed.

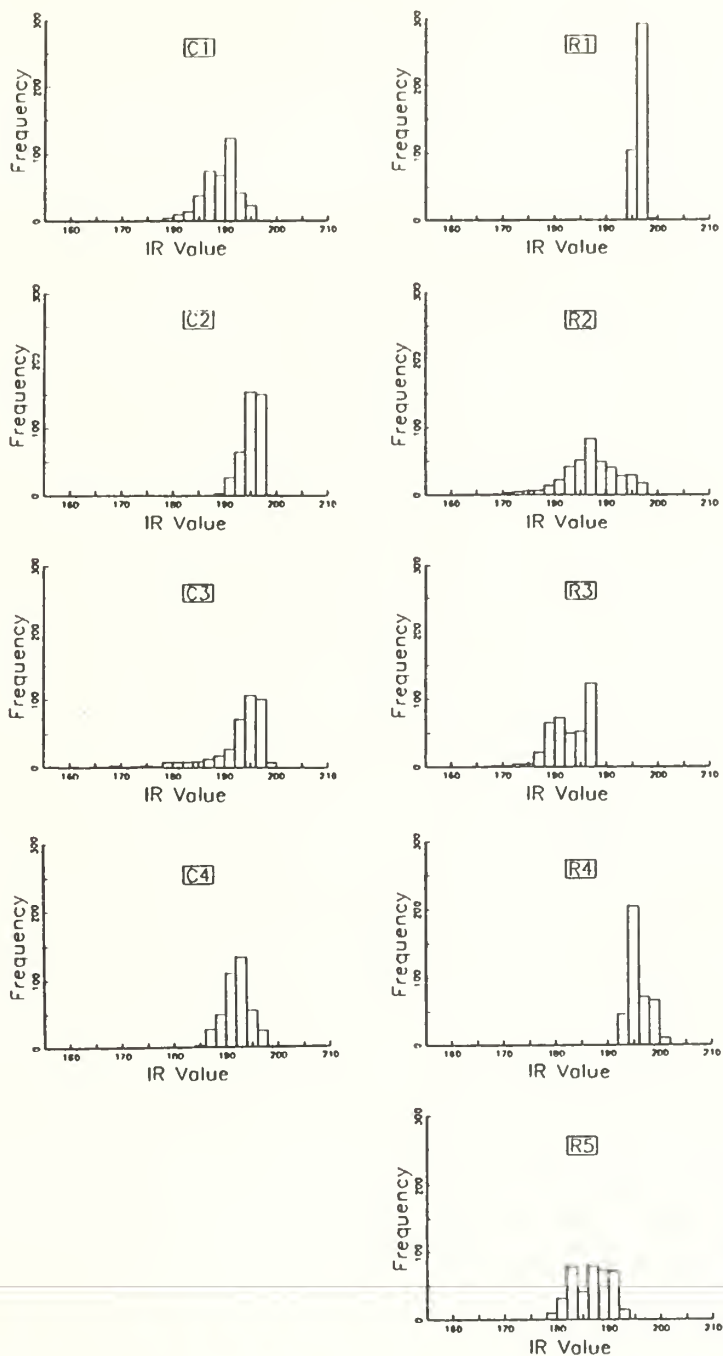


Fig. 9 As for Fig. 6, except Case B.

Figure 9 shows that, like Case A, the cirrus boxes have a more Gaussian distribution than the rain boxes. However, a wide range of standard deviation and kurtosis values is present for both groups. This case illustrates the large differences that can exist for different cases.

C. CASE C: 4/2101 JANUARY 1989

Case C satellite imagery (Figures 10 and 11) illustrates precipitation and cloud structure of the IOP 4 cyclone, the deepest extratropical cyclone of the experiment (Hartnett et al. 1989). The system first appeared as several low centers off the North Carolina coast, then deepened into a powerful, single center cyclone when a strong upper-air disturbance reached the coastline at about 4/0000. Rapid intensification occurred between 4/0900 and 4/1500, with an estimated deepening rate of 24 mb/6 h. The cyclone continued to develop as it moved northeast towards Newfoundland. At the time of Case C imagery, the cyclone is centered at 39N 59W, with a central pressure of 950 mb. This case differs from the others in that the system is mature, vice incipient, with pronounced frontal structure at the time of the imagery.

The 4/2101 GOES IR imagery (Figure 11) includes the labeled cirrus and rain cloud boxes to be statistically analyzed. Again, these boxes were chosen on the basis of SSM/I determined rain/no-rain areas (Figure 10). The 4/2147 SSM/I imagery for this case was not concurrent with GOES, but differs by 46 min. The time difference is not considered significant for this analysis because the size and location of the cloud boxes, well buffered by surrounding areas of similar SSM/I and IR values, more than accounts

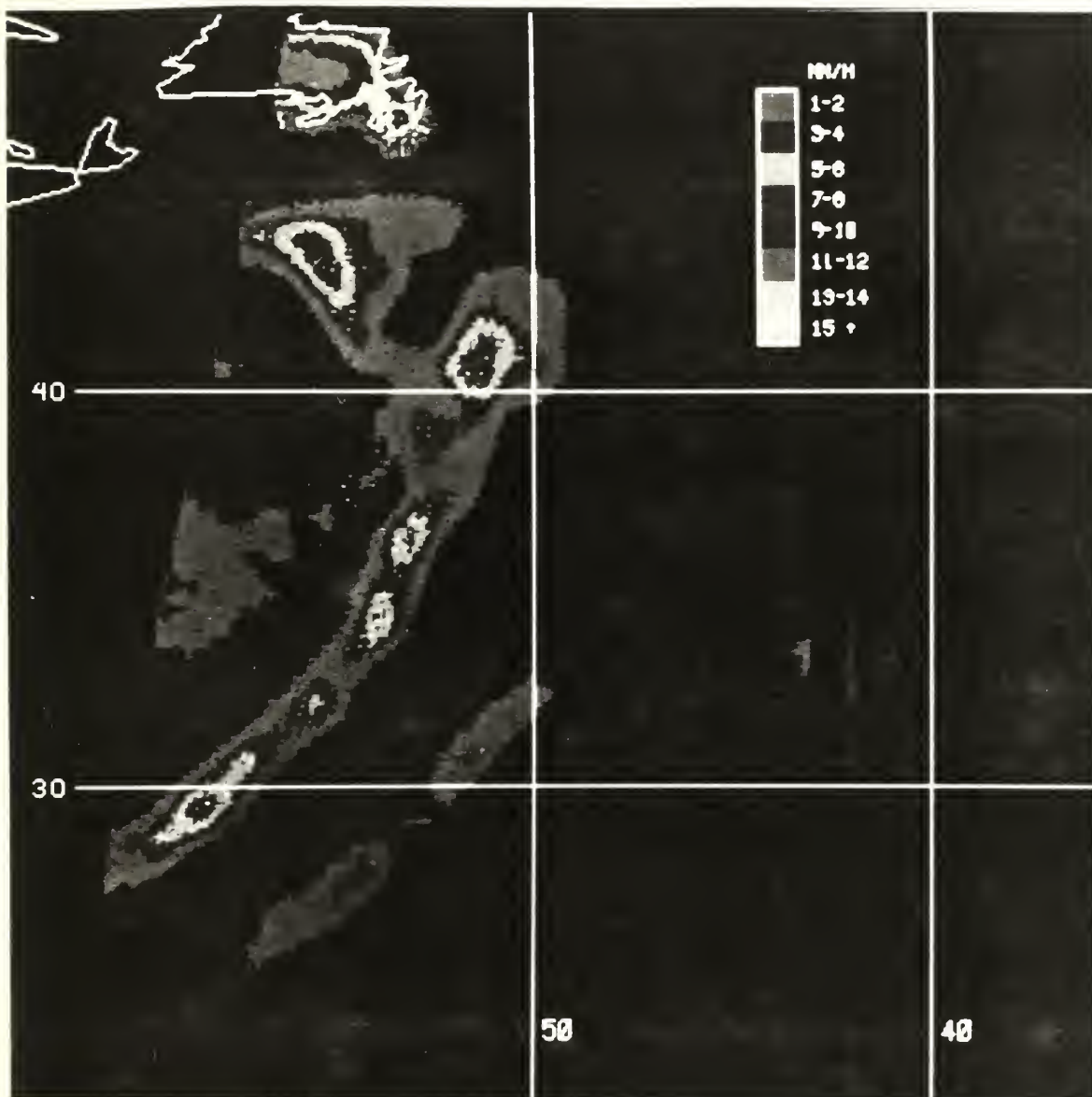


Fig. 10 As in Fig. 4, except Case C: 4/2147 January 1989.

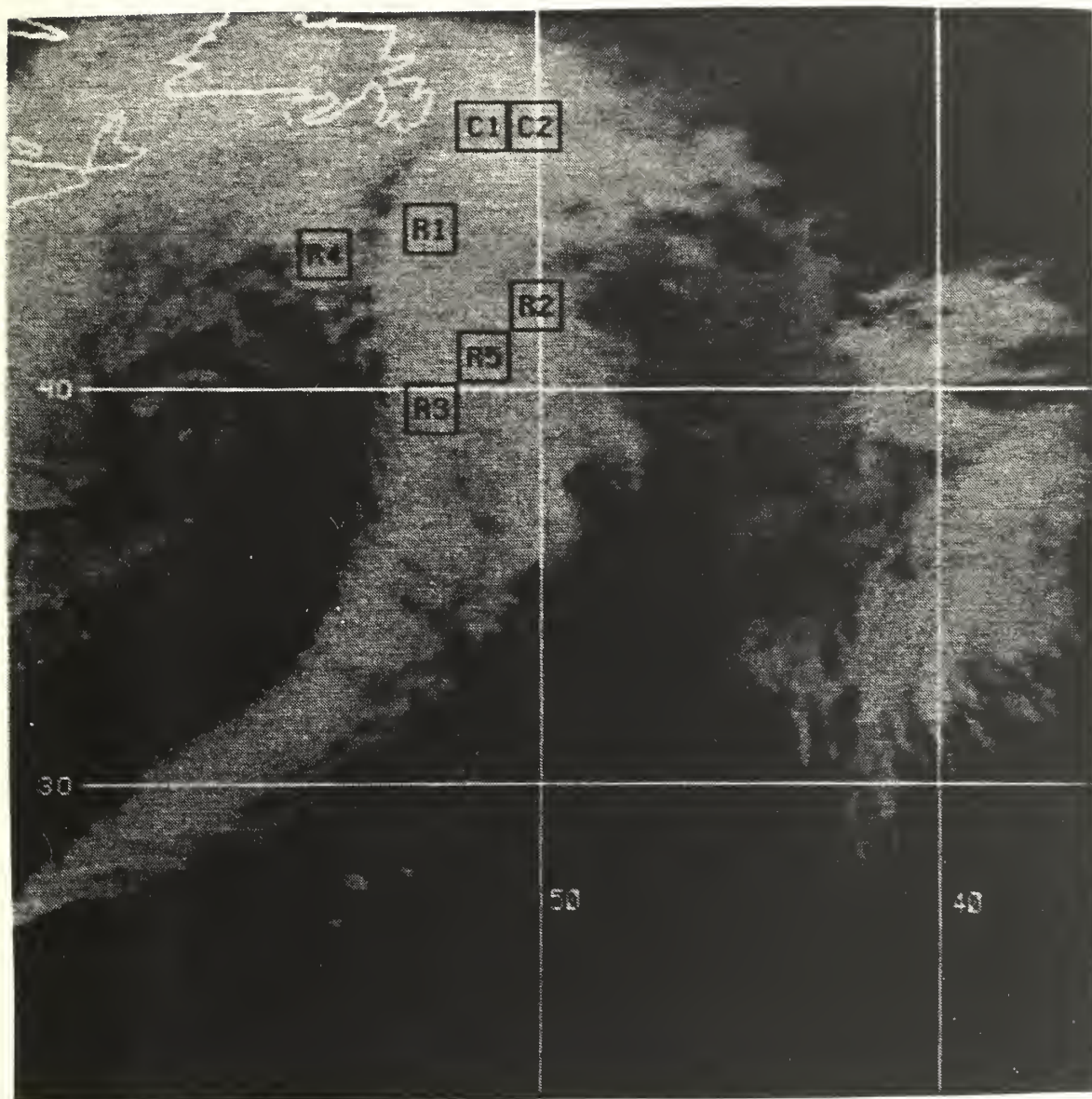


Fig. 11 As in Fig. 5, except Case C: 4/2101 January 1989.

for any movement or development of the cyclone system. Restricted by swath width, the SSM/I imagery shows the comma tail and NE area of the comma head, but not the cyclone center.

Table IV CASE C SAMPLE STATISTICS

Box	Rainrate	Mean	Std.Dev.	Kurtosis
C1	0	185.83	5.14	3.90
C2	0	186.76	4.86	2.78
Mean C		186.30	5.00	3.34
R1	Lt	194.97	2.81	2.75
R2	Lt	186.87	3.46	2.66
R3	Lt/Mod	197.14	3.15	3.11
R4	Hvy	186.45	5.13	3.95
R5	Hvy	192.21	3.95	1.97
Mean R		191.53	3.70	2.89

Distribution histograms are depicted by Figure 12, and sample statistics by Table IV. As in Case A, mean IR value is the parameter which most strongly discriminates cirrus from rain samples. Cirrus samples exhibit a mean IR value of 186.30, compared to a value of 191.53 attributed to rain samples. While distinguishable, this difference is not as significant as that shown in Case A. The histograms show a strong distribution similarity between the two cirrus boxes. And while the distributions for R1, R3, and R5 are similar, there is no clear grouping of values for light, moderate, or heavy rain. Standard deviation values are generally less for rain samples than cirrus samples, and again, kurtosis values show no consistent differences.

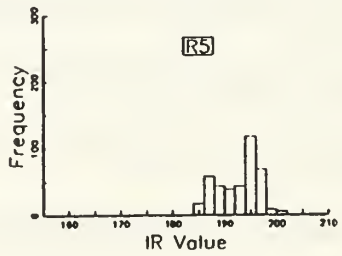
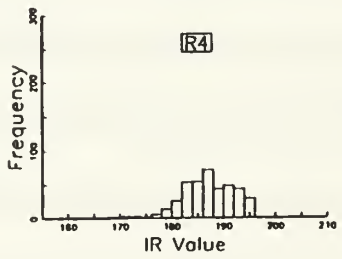
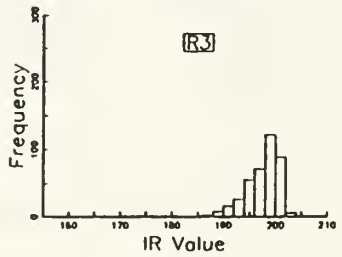
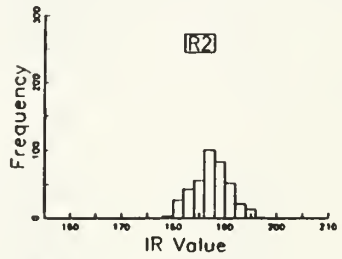
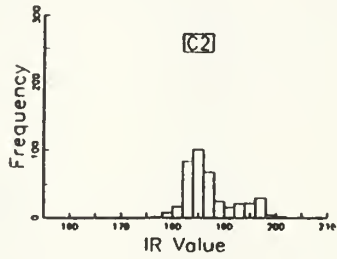
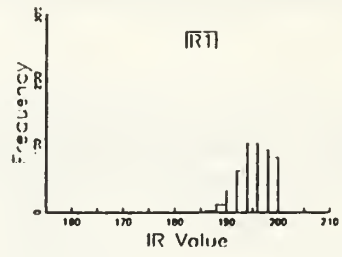
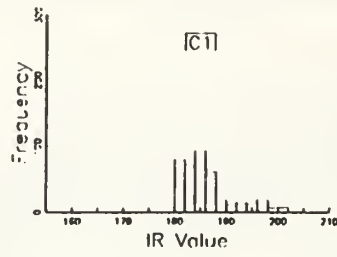


Fig. 12 As in Fig. 6, except Case C.

D. OVERALL RESULTS

Cases A, B, and C documented variations between non-raining and raining cloud areas of several cyclones. The cloud boxes describe the distribution of IR values within each area and the variables mean, standard deviation, and kurtosis.

In general, mean IR count proved to be the strongest delimiter of rain from cirrus. In Cases A and C, rain box means were notably higher than cirrus box means. This was not evident in Case B, however, where cirrus means were slightly higher than rain means. Standard deviation also appeared to have some value in discriminating rain from cirrus boxes. Overall, light/moderate rain exhibited the lowest values, cirrus the intermediate values, and heavy convective rain the highest values of standard deviation. These findings are somewhat in accord with those of Adler and Negri (1988). In discerning cirrus areas from thunderstorm (strong convection) areas, Adler and Negri attributed warmer cloud top temperatures and lower standard deviation values to cirrus areas. Because no description of neighboring light/moderate rain areas was given, it is unclear if discrimination between cirrus and non-convective rain is possible with this method. Adler and Negri's work was based on tropical convective systems, whereas the ERICA storms were mid latitude cyclones.

Kurtosis values were examined as a means to describe the peakedness of the distribution histograms. This parameter, however, demonstrated no consistent pattern in separating cirrus from rain.

Synoptically, a certain precipitation pattern is evident from the SSM/I precipitation analyses. Heaviest rain areas, associated with strong convection, lie near the cyclone center, and are also evident along frontal bands. These areas are usually ringed by areas of moderate, then light rainfall. From the analyses above, the light/moderate rainfall can be reasonably identified in the IR by high mean and low standard deviation. Heavy convective rainfall is not so readily identified in the IR. However, areas central to the cyclone ringed by light/moderate rain areas which exhibit "ragged" IR values (lower mean, high standard deviation) can realistically be presumed to be convective rain. Cirrus cover, then, appears to be the limiting factor in using IR data to identify rain areas. Less accuracy can be expected for IR prediction schemes applied to cases with widespread cirrus blowoff. Cirrus identification could be achieved by the incorporation of data from VIS (Lovejoy and Austin 1979a) or split-window IR channels (Neu 1990) into the scheme.

The analyses above were based on a limited number of hand-selected cloud boxes. While the results suggest that the IR value mean and standard deviation may be used to discriminate rain from no rain areas, the number and selective choice of sample cloud boxes do not yield statistically significant results. The following chapter discusses the logical extension of this analysis, where a large number of smaller cloud boxes, systematically chosen from the satellite imagery, is analyzed using discriminant analysis techniques.

V. DISCRIMINANT ANALYSIS APPROACH

The preliminary analyses of the cloud boxes in Chapter IV indicated that IR mean and standard deviation could discriminate rain from no-rain areas. A discriminant analysis was performed to statistically determine if these variables could be used over the entire IR image to classify precipitation.

A. DISCRIMINANT ANALYSIS THEORY

Discriminant analysis is a statistical procedure for identifying the boundaries between groups in terms of the variable characteristics that distinguish one group from another. The procedure is used to classify events by finding the combination of variables that best predicts the category or group to which a case belongs. For this analysis, events (10 x 10 pixel IR cloud areas) will be classified into categories (rain or no-rain) on the basis of three variables (IR mean, standard deviation, and kurtosis).

The simplest and most commonly used method is Fisher's linear discriminant analysis (Fisher 1936). This method finds the coefficients a_1 , a_2 , and a_3 so that the linear discriminant scores,

$$D = a_1X_1 + a_2X_2 + a_3X_3$$

for each group are maximally separated. For this analysis, the variables represented by X_1 , X_2 , and X_3 are mean, standard deviation, and kurtosis. Because the population is

partitioned into only two groups (rain and no-rain), a single discriminant function is sufficient for classification.

It is possible to adjust the distance criterion to account for prior information about the likelihood of an event (prior probability) and for unequal misclassification costs. If a particular misclassification error is especially undesirable (eg. over-prediction vs. under-prediction of rain area), then a higher penalty for that error would be incorporated into the discriminant function. In order to compare the results to others, the discriminant functions in this study are computed assuming uniform prior probabilities and equal misclassification costs. That is, an area has an equal probability of being classified as rain or no-rain, and misclassification in either direction carries the same penalty.

Discriminant functions are determined from a data set termed "development data." Cross-validation is a method of testing the discriminant (or classification) function on an independent data set, termed "validation data."

B. PROCEDURE

For each case (A, B, and C), remapped SSM/I and IR imagery was divided into 10 x 10 pixel boxes. The NPS IDEA Lab was used to display the imagery and select a data set of 10 x 10 boxes which meet all the following criteria:

1. Area is oceanic.
2. SSM/I analysis yields either no-rain (0 rain pixels) or rain (at least 70% raining pixels). Thus, rain border areas are eliminated.

3. All GOES IR pixels within a box describe mid to high cloud top temperatures (IR count at least 153, 253.5 K or colder, after Negri and Adler 1988).

A data sample set of 166 boxes was obtained for Case A, 124 boxes for Case B, and 176 for Case C. Computational efficiency is increased by restricting the analysis to areas consisting of mid to high clouds, where a high probability of rain exists. Little SSM/I rain was associated with cloud top temperatures warmer than 253 K for these ERICA oceanic storms, where areas of light (1-2 mm/h) post-frontal and stratiform rain were sparse. The exclusion of clear sky and low cloud areas, where rain/no-rain delineation is inherently simple, does reduce the statistical success of the scheme.

For each sample box, the SSM/I-determined rain/no-rain category was recorded for use as ground truth. IR values were evaluated, and the mean, standard deviation and kurtosis determined for each box. Table V presents a synopsis of the data used in the discriminant analysis procedure. Mean values of each of the three variables are shown for the rain and no-rain categories. In all three cases, little difference is seen in standard deviation and kurtosis values. That is, the standard deviation for each of the two variables exceeds the difference between the actual standard deviation and kurtosis means for the rain and no-rain categories. Values of mean show the greatest variation between rain and no-rain samples, indicating that the IR temperature itself may be the strongest variable for classification purposes.

One way to visualize the distribution or separation of the rain/no-rain categories in terms of the discriminating variables is with a scatterplot. Figure 13(a) presents such

Table V CLASSIFICATION VARIABLES. Mean values for each of the rain/no rain classification variables are indicated.

Case	SSM/I Category	No. of Samples	Mean	Std. Deviation	Kurtosis
A	Rain	116	194.82	3.40	3.46
	No Rain	50	185.32	3.15	3.29
B	Rain	77	188.88	2.15	3.29
	No Rain	47	189.57	2.43	3.51
C	Rain	88	192.13	3.35	3.16
	No Rain	88	184.84	3.85	3.60

a plot, illustrating Case A's rain/no-rain distribution as a function of all three variables. "1" and "2" represent no-rain and rain categories, respectively. The plot suggests the separation of the two categories, primarily along the axis given by the IR mean. Figure 13(b) is a two dimensional plot which shows the separation of the rain/no-rain categories as a function of two variables. Again, IR mean is the strongest discriminating variable. However, this plot reveals a significant role of standard deviation in the separation of rain/no-rain, particularly where IR mean values range from 180 to 194 (238-224 K). In this range, rain areas exhibit higher standard deviation values than no-rain areas. A similar observation was made by Adler and Negri (1988), who found that at intermediate temperatures (235-215 K), thunderstorm areas had a tighter gradient around their temperature minima than did cirrus areas. A measure of standard deviation, this gradient was termed the "slope parameter" by Negri and Adler.

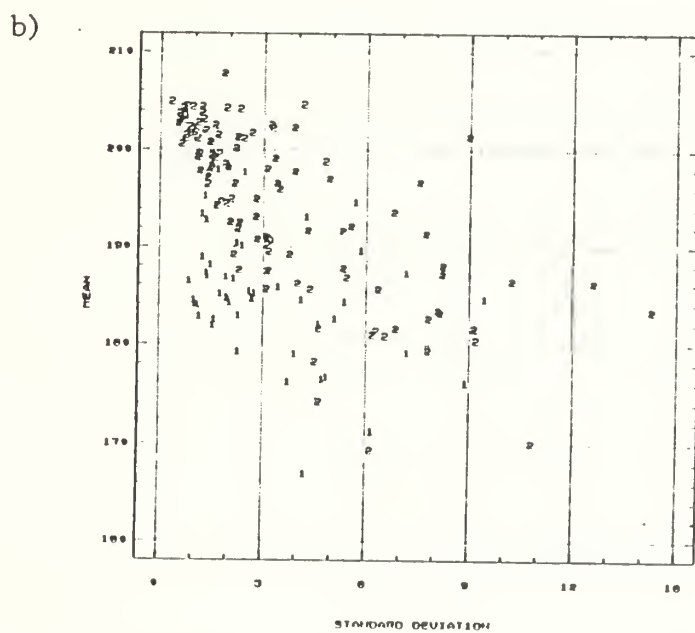
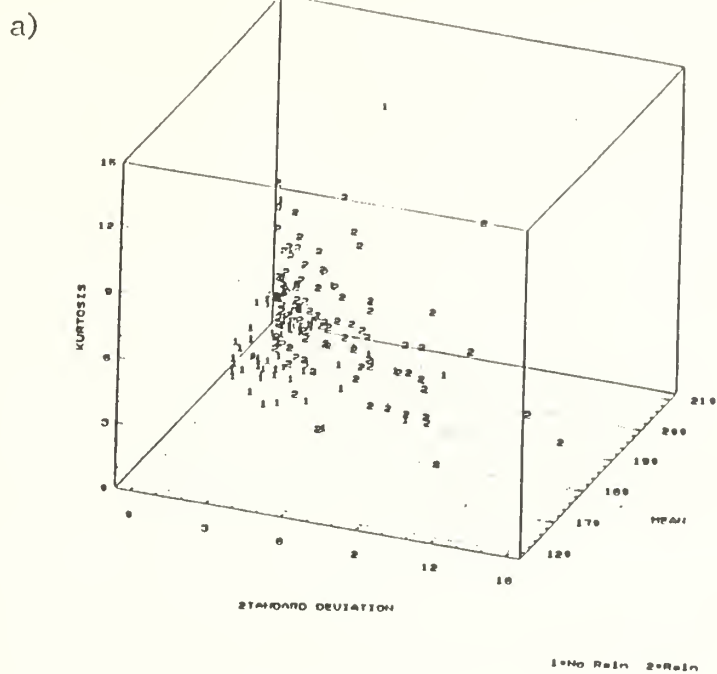


Fig. 13 Scatterplots showing distribution of Case A rain/no-rain areas as functions of
a) IR mean, standard deviation and kurtosis; b) IR mean and standard deviation.
"1" represents no-rain, "2" represents rain.

While the scatterplots graphically indicate separation of the rain/no-rain categories, the role of discriminant analysis is to quantify that separation in terms of the three variables. Development and validation data sets were prepared in order to determine and test the discriminant functions. One fourth of the samples from each data set was randomly withheld for use as validation data, while the remaining three fourths constituted the development data. Using Statgraphics 4.0 PC software, linear discriminant analysis was performed on each case's development data. SSM/I rain/no-rain category was the "classification factor," and IR value mean, standard deviation and kurtosis constituted the "classification variables." Uniform prior probabilities were assumed. The analyses determined a discriminant function for each case, classifying the development data accordingly. Table VI illustrates the success of this classification, showing percentages of correctly classified categories. Cross-validation was performed by applying the discriminant functions to the validation data sets, and events were classified with the success rates noted in Table VI.

C. CLASSIFICATION RESULTS

1. Rain / No-Rain Classification

As was evident in the previous chapter's cloud box study and the scatterplots shown in Figure 13, Case A shows reasonably clear separation between rain and no-rain samples. Rain boxes were correctly identified 78% of the time. This equates to POD and FAR scores (Tsonis and Isaac 1985) of 0.78 and 0.09, respectively (a perfect

Table VI LINEAR DISCRIMINANT ANALYSIS RESULTS. Results indicate percentages of categories correctly identified by the discriminant function.

Case	Category	Development Data (% Correct)	Validation Data (% Correct)
A	Rain	79.54	78.57
	No Rain	81.58	83.33
B	Rain	50.85	50.00
	No Rain	70.59	53.84
C	Rain	73.24	58.82
	No Rain	69.23	56.52

scheme yields $POD = 1$ and $FAR = 0$). There is little difference between the scores obtained from the development and validation data, indicating that the discriminant function is valid for independent data. Operationally, this suggests that a classification function determined for coincident SSM/I and GOES satellite images is applicable to subsequent GOES images.

Scores for Case B indicate that the discriminant function has little skill in classifying rain samples. Success rates near 50% are no better than random choices. Scores for classification of no-rain samples are reasonable for development data, but decrease to near-random for validation data. The previous chapter's cloud box study revealed the mean IR value of the cirrus boxes to be slightly higher than that of the rain boxes. This observation is confirmed in this more encompassing analysis (Table V). Considering the relatively large variance about the mean for the variables IR mean, standard deviation and kurtosis, little difference is seen between the rain and no-rain

values for any of the three classification variables. This suggests a low success rate for any discriminant function applied to this case.

Case C scores show reasonable skill in classification of development rain and no-rain data samples. Rain classification scores translate to POD and FAR scores of 0.73 and 0.30, respectively. However, skill scores decrease significantly when the validation data is used, indicating that the classification scheme has less validity beyond the coincident SSM/I and GOES data set.

For this analysis, the three classification variables mean, standard deviation, and kurtosis were incorporated into the discriminant functions. Because the value of kurtosis as a classification factor was in question, discriminant functions were then determined using combinations of two of the three variables listed (discriminant analysis requires at least two variables). Classification results from these various functions indicate very limited value of kurtosis in rain/no-rain discrimination. Confirming the implications of Table V, IR mean is, by far, the strongest classification variable. Standard deviation also is of value, but to a lesser extent. Similar observations were made by O'Sullivan et al. (1990), who tested up to 16 first and second order image statistics as discriminating variables for precipitation estimation. They found their best results when using a simple model incorporating only the mean and standard deviation. For operational efficiency, then, discriminant analysis for rain/no-rain classification should be performed using only IR mean and standard deviation. The dominant role of the IR

mean cloud top temperature in rain/no-rain classification indicates that an even simpler method using only IR count, may yield similar scores. Such a method is explored in Chapter VI.

2. Further Division of Rain Categories

The classification results shown in Table VI indicate that discriminant analysis can be used to classify rain and no-rain events, with resultant skill levels dependent on the case. Chapter IV's cloud study indicated, for Case A, that categories of rain intensity might also be identified. Several authors have attempted, with varying success, to expand their rain/no-rain delineation schemes to classify rain intensity categories. Negri and Adler (1987a) found that useful, accurate rainfall estimates beyond rain/no-rain discrimination were unlikely with their IR technique. However, O'Sullivan et al. (1990) found moderate success in classifying light and moderate/heavy rainfall with an IR/VIS scheme. Most of the studies worked with over-land precipitation, using radar as ground truth. Here, the possibility of rain intensity classification for oceanic areas using microwave ground truth is explored.

Data samples for each case were analyzed by the SSM/I exponential algorithm to be either no-rain (<1 mm/h), light (1-2 mm/h), moderate (2-4 mm/h), or heavy rain (>4 mm/h). Again using the three IR variables with uniform prior probabilities and equal misclassification costs, discriminant functions were determined. The classification results, averaged for Cases A, B, and C, are presented in Table VII.

Table VII RAIN INTENSITY CLASSIFICATION RESULTS. Results indicate averaged (Cases A, B and C) percentages of rain categories identified by the discriminant functions. Shaded boxes are categories correctly classified.

		IR Predicted			
		No Rain	Light	Moderate	Heavy
SSM/I Observed	No Rain	51.0	15.8	16.8	16.3
	Light	19.9	17.1	33.2	29.7
	Moderate	11.4	20.8	33.3	34.6
	Heavy	14.6	12.2	25.4	47.8

The effect of further dividing the rain categories is to significantly reduce the skill scores for all categories. While no-rain identification is achieved with reasonable (but reduced) skill for Cases A and C, 85% of Case B's nonraining events are misclassified as rain. Table VII's shaded boxes show percent correct classification of rain intensity categories, which ranges from 17.1 to 51.0. The no-rain and heavy rain categories are the most successfully classified, while light and moderate rain are more often than not misclassified. Results of this analysis indicate that further discrimination beyond rain/no-rain categories is not feasible with a single IR channel discriminant analysis scheme.

VI. OPTIMAL THRESHOLD APPROACH

Chapter V showed that discriminant analysis could be used with some success to delineate rain from no-rain areas. The primary discriminators were IR mean and standard deviation, although most of the separation was accounted for by IR mean. These results suggest that a more operationally efficient scheme utilizing an optimal IR threshold value may yield similar rain/no-rain results. Tsonis (1988) found that a single VIS or IR thresholding scheme was quite adequate in delineating rainfall from satellite imagery. Compared to more complicated schemes, little accuracy was lost, and was more than compensated for in increased flexibility, speed and economy. The objective of this approach is to determine an optimal IR threshold value by optimizing a set of statistical parameters.

A. PROCEDURE

The 512 x 512 pixel arrays of the remapped SSM/I and IR imagery were scanned with a FORTRAN program on the NPS IDEA Lab. For each oceanic, mid/high cloud pixel, the rainrate (derived from the SSM/I exponential rainrate algorithm) and coincident IR value were recorded in a new array. As with the discriminant analysis approach (Chapter V), analysis is restricted to areas containing mid/high clouds, defined by an IR value of 153 (253.5 K) or colder (after Negri and Adler 1987b) to increase computational efficiency and to focus on the overcast rain/no-rain problem.

An IR threshold value was defined such that any IR value equal to or colder than the threshold value was assumed to be rain. Threshold values were chosen iteratively, beginning with 153 and spanning the full range of IR values obtained (up to 210). All evaluation statistics were calculated for each IR threshold. The SSM/I threshold remained constant - any value equal to or greater than 1 mm/h was defined as rain, anything less as no-rain.

Given the IR and SSM/I thresholds, all pixels were assigned to one of the four boxes in the precipitation contingency table, Table VIII (following the classifications defined by Lovejoy and Austin, 1976). SSM/I classifications are considered to be "ground truth." Thus, the IR classification's correctness is judged by its agreement with the SSM/I analysis.

Table VIII PRECIPITATION CONTINGENCY TABLE (after Lovejoy and Austin 1976)

		IR Prediction	
		Rain	No Rain
SSM/I Classification	Rain	HIT	MISS
	No Rain	FALSE ALARM	DRY

The four IR classifications are:

1. Hit - correctly classified as rain
2. Miss - incorrectly classified as no-rain

3. False Alarm - incorrectly classified as rain
4. Dry - correctly classified as no-rain

Following Donaldson et al. (1975) and Tsonis and Isaac (1985), several measures of success or error were calculated from this contingency table (see Appendix A for equations). Briefly defined, those measures are:

1. Probability of Detection (POD) - gives ability of scheme to "find" the rain
2. False Alarm Ratio (FAR) - measures the proportion of incorrect rain predictions
3. Critical Success Index (CSI) - compromise score to balance the need for maximal Hits against disadvantages of excess False Alarms
4. Percent Error (ERR) - measures the error in rain area delineation over the total area analyzed
5. Areal Error (AREA) - measures the percent difference between observed (SSM/I classified) and IR predicted rain areas

B. EVALUATION

The optimal IR threshold is that value which yields the optimal combination of the success measures described. A perfect rain delineation scheme would give $POD = 1$, $FAR = 0$, $CSI = 1$, $ERR = 0$, and $AREA = 0$. None of these statistics can be used alone, however, as none is necessarily more representative of the scheme's success than any other. Rather, each statistic gives additional information about the effectiveness of the rain delineation scheme.

For instance, a threshold could create a rain area five times its actual size, and still give a POD of one. To be meaningful, a high POD should be accompanied by a low

FAR. CSI takes this into account somewhat, by combining the POD and FAR scores into a single compromise score. However, the relative costs of Miss (rain under-predicted) versus False Alarm (rain over-predicted) errors may vary for each operational user, and should be considered in the weighting of terms in the CSI calculation. For this study, CSI is calculated assuming equal misclassification costs (i.e. Miss and False Alarm errors carry the same penalty). Because ERR represents the error in rain area delineation with respect to the entire area analyzed, a good (low) ERR score can be obtained even with poor POD and FAR scores, if the precipitation area is small. And, while a low AREA score means that the observed rain area nearly equals the predicted area in size, the scoring does not mean that the two areas are colocated. Because there is no one preferred score, all of the statistics should be considered in the development of a scheme, with emphasis placed on those statistics which suit the needs of the particular user.

Ideally, the optimal IR threshold would be that which yielded minimum values of ERR and AREA, and maximum values of CSI. Setting a critical value of POD would indicate the minimum level of success acceptable in actually "finding" the rain areas. The following section describes how the optimal threshold scheme fared with Cases A, B, and C.

C. RESULTS

Figure 14 illustrates how the evaluation statistics POD, FAR, CSI, ERR and AREA varied as a function of IR threshold value for the three cases studied. As

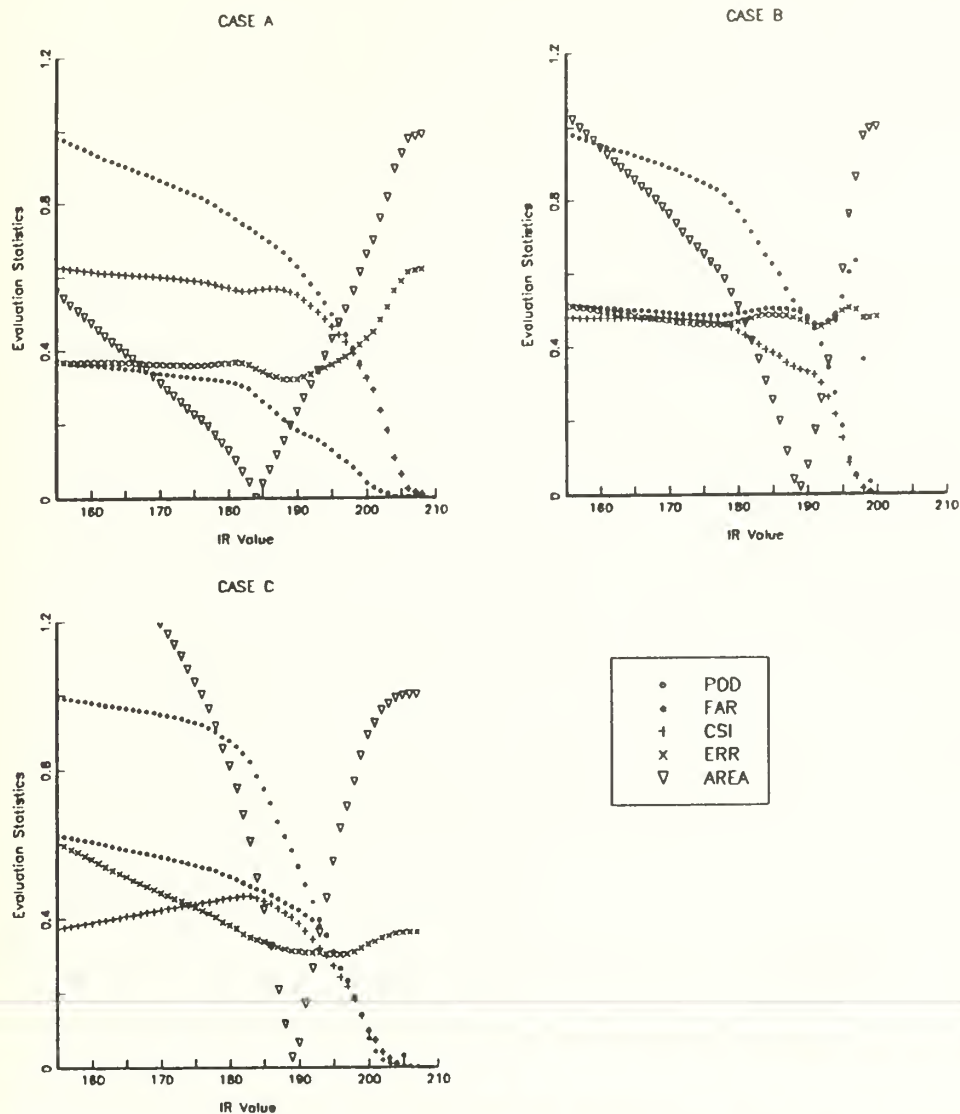


Fig. 14 Evaluation statistics POD, FAR, CSI, ERR and AREA as functions of IR value for Cases A, B, and C.

expected, POD and FAR scores decreased with increasingly colder IR threshold values (except in Case B, where FAR scores were nearly constant). It was anticipated that, by combining the POD and FAR scores into a compromise CSI score, a min/max pattern

would emerge which allowed determination of the optimal threshold determination at the CSI maximum. Unfortunately, such a pattern was not evident in Cases A and B. Instead, CSI scores showed a wavering decreasing trend with colder IR threshold values. Slight relative mins and maxes were apparent, but scores remained nearly constant below IR counts of 195 (Case A) and 190 (Case B). Case C, however, did exhibit a modest min/max pattern. Because the CSI score yielded unexpectedly limited information, a minimum acceptable POD was established. Such a POD would not only aid in obtaining an IR threshold value, but would enable comparison of the scheme's results with those of other techniques. An average POD of 0.62 was obtained from the discriminant analysis validation data sets in Chapter V. In accordance with this value, a minimum acceptable POD of 0.60 was established for the optimal threshold analysis.

Figure 15 shows the pattern of the evaluation statistics POD, ERR and AREA for the three cases analyzed. Statistics are plotted against increasingly colder IR threshold values. Although one's eye may be drawn to the junction of the three curves as a choice for the optimal threshold, the goal is to find an IR value that best coincides with minimums in the ERR and AREA curves and still yields an acceptable POD score.

Table IX is presented to compare the statistical results of the optimal threshold approach with those of the discriminant analysis approach.

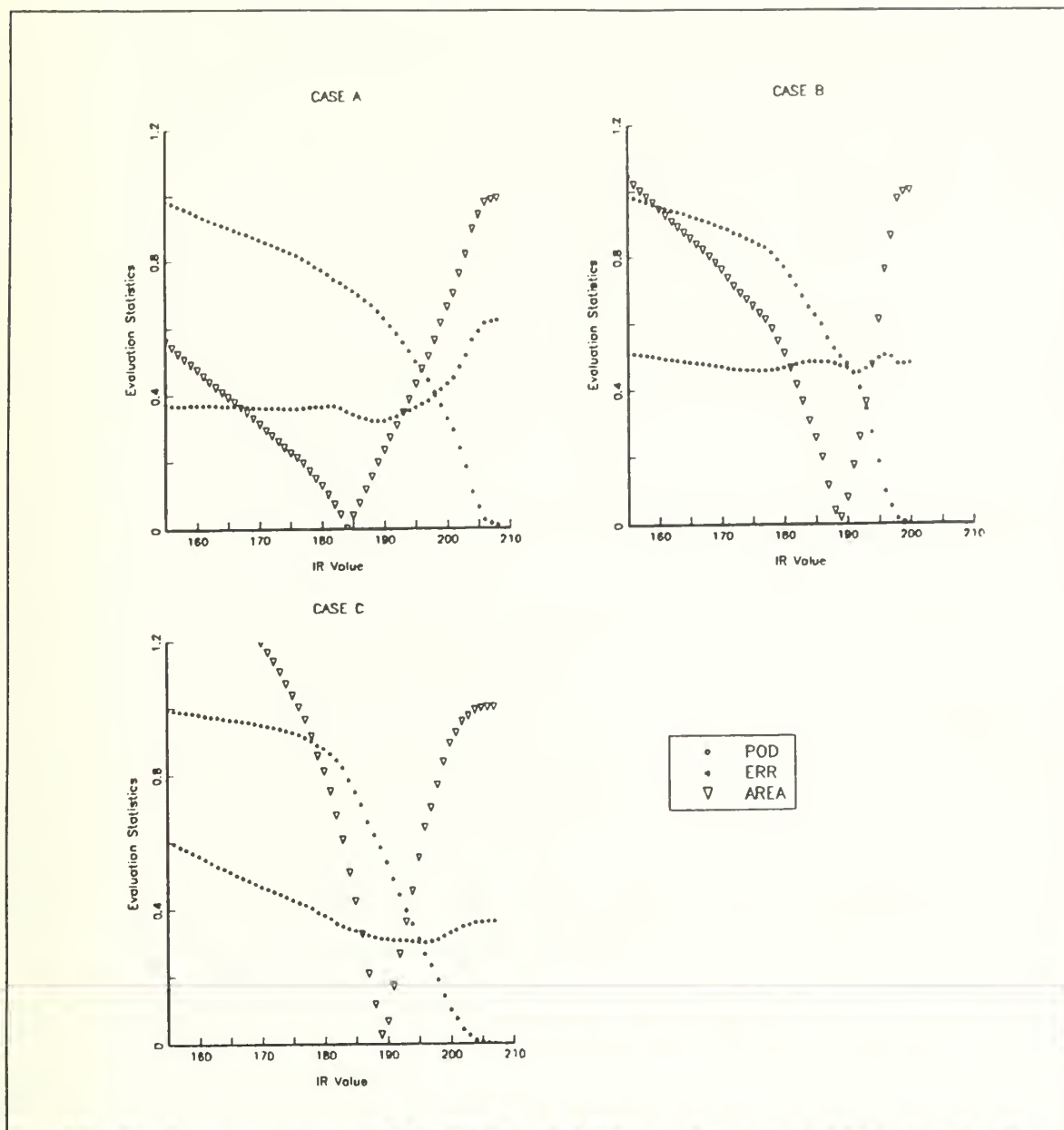


Fig. 15 Evaluation statistics POD, ERR and AREA as functions of IR value for Cases A, B, and C.

1. Case A: 13/0901 December 1988

Figure 15 shows clear minimums for both ERR and AREA scores for Case A. The ERR curve is relatively flat for IR values below 181, dips from IR values of 181 to 189,

Table IX COMPARISON OF STATISTICAL RESULTS. Optimal threshold vs. average (development and validation data) discriminant analysis.

Case	Statistic	Optimal Threshold	Discriminant Analysis	
			(Devel.)	(Valid.)
A	POD	.70	.80	.79
	FAR	.25	.09	.08
	ERR	.33	.20	.20
B	POD	.60	.51	.50
	FAR	.50	.25	.40
	ERR	.48	.42	.48
C	POD	.62	.73	.59
	FAR	.44	.28	.50
	ERR	.32	.29	.42

and then rises steadily with increasingly colder values. The min ERR score of 0.32 corresponds to an IR value of 189 (229 K). The AREA curve exhibits a V-shaped pattern, reaching 0.0 at an IR value of 184 (234 K). At this value, IR predicted rain area is equal to (but not necessarily coincident with) SSM/I predicted rain area. For lower (warmer) IR values, predicted rain area exceeds observed rain area. The reverse is true for IR values higher (colder) than 184.

Because no one IR value corresponded to both ERR and AREA mins (189 and 184, respectively), a median value of 186 (232 K) was chosen as an optimal threshold for Case A. This value is midway between the ERR and AREA min locations and also corresponds to a weak relative max in CSI (0.57), seen in Figure 14. A POD score of 0.70 is obtained, well exceeding the POD threshold of 0.60. At this IR value, ERR and AREA scores vary little from their minimums. The optimal threshold is one degree colder than the mean temperature of the cirrus boxes found in Chapter V (Table V).

Compared to the discriminant analysis method, the optimal threshold scheme yielded less satisfactory results for Case A. Besides the obvious differences in statistical analysis, it is important to note the differences in sampling technique between the two methods. While the optimal threshold pixels met the same oceanic, mid/high cloud criteria as the discriminant analysis boxes, the averaging procedures smoothed the data and allowed for the elimination of rain border areas in the discriminant analysis method. Additionally, because individual pixels (vs 10 x 10 pixel boxes) were evaluated, the optimal threshold sample sets were two orders of magnitude larger than the discriminant analysis sample sets.

2. Case B: 13/2301 December 1988

The ERR curve for Case B is reasonably flat throughout, but fluctuates modestly for IR values colder than 180. The minimum ERR score of 0.45 is found at the IR value of 191 (227 K). As in Case A, the AREA curve is V-shaped, reaching 0.0 at an IR value of 189 (229 K). A reasonable choice for the IR threshold, then, would appear to be the median value of 190 (228 K). However, this yields a POD score below the minimum acceptable score of 0.60.

As the slopes of the POD curves in Figure 15 show, higher POD values are obtained at lower (warmer) IR values. For this case, the threshold was moved to progressively warmer temperatures until an acceptable POD score was obtained. An optimal IR threshold value of 186 (232 K) was chosen for Case B, giving a POD level of 0.60. As in Case A, the choice of a compromise value yields little deviation of ERR

and AREA scores from their minimums, suggesting a possible "window" of optimal threshold values. Case B is complicated by the abundance of extremely cold cirrus associated with the jet stream. Table V showed that cirrus sample means were slightly colder than rain sample means, indicating that the use of IR value to determine rain area would be limited in this case. For Case B, optimal thresholding produces superior results to discriminant analysis. Optimal thresholding was the only scheme able to produce an acceptable POD level, and although the FAR was higher (in proportion to the increased POD), ERR scores were held nearly constant.

3. Case C: 4/2101 January 1989

Unlike the previous cases, which exhibited nearly flat ERR score curves at low (warmer) IR values, Case C's ERR scores decrease constantly with colder values until reaching a minimum value of 0.30 at an IR value of 194 (224 K). The ERR curve rises slightly at colder IR values. The AREA curve again exhibits a V-shaped pattern, reaching 0.0 at an IR value of 189 (229 K). As in Case B, all choices of intermediate IR threshold values (between 189 and 194) yield POD scores below 0.60. The nearest IR value which yields an acceptable POD score of 0.62 is 188 (230 K). Again, near minimum values of ERR and AREA are seen at this compromise IR threshold.

Compared to the discriminant analysis (validation data) results for Case C (Table IX), the optimal threshold scheme produced better (lower) FAR and ERR scores, while still attaining an acceptable POD. In this case the division between cirrus and rain IR

values is evident and useful. In fact, the optimal IR threshold value of 188 is equal to the midpoint between the cirrus and rain sample IR means (184 and 192) found in Chapter V.

In summary, the following steps were taken to determine the optimal IR threshold value for the cases analyzed:

1. Determine IR value corresponding to minimum ERR score.
2. Determine IR value corresponding to minimum AREA score.
3. If IR values are not the same, chose intermediate value.
4. Evaluate POD score for IR value obtained in step 3. If POD meets or exceeds pre-determined acceptable level, use this IR value as optimal threshold. If POD is below acceptable level, move to warmer threshold, choose nearest IR value that yields acceptable POD.

4. Case Comparisons

In comparing the pattern of evaluation statistics in Cases A, B and C, several features are noticeable. In all three cases, the min AREA score yields a lower IR threshold value than does the min ERR score. Whereas the AREA curve exhibits a consistent V-shaped pattern, the shape of the ERR curve varies from case to case. POD scores decrease with increasingly colder IR threshold values, but the slope of the POD curve varies with each case.

In none of the cases did a single IR threshold value coincide with sufficient POD and minimums in both ERR and AREA, so compromise thresholds were selected. The thresholds chosen were within three degrees Kelvin of the value corresponding to the

AREA min. Little variation was seen in the ERR and AREA values from their min values, suggesting that an optimal threshold window exists.

Threshold values of 186, 186, and 189 were chosen for Cases A, B, and C, respectively. These values correspond to a cloud top temperature range of 229 K to 232 K. Studies by other authors have revealed a variety of threshold values. Negri et al. (1984) used an IR threshold of 228 K to describe the 50% coldest area (rain threshold). When using single-value IR thresholding, Negri and Adler (1987b) found their best results with a value of 240 K, while Tsonis (1988) found that a 245 K threshold yielded optimal results. It is expected that the value be case-dependent, depending on the location, development and dynamics of each rain producing system.

While the threshold is valid only for the particular system, it should be applicable for several hours of GOES imagery. Optimal threshold values were applied to subsequent GOES IR imagery for the three cases analyzed, yielding rain patterns consistent with synoptic expectations. Figures 16 through 23 in Appendix B show the rain patterns obtained when the optimal IR threshold of 232 K is applied to successive GOES IR imagery for Case A through Case B. The rain area pattern for the Case A system moves east until out of range of the GOES imagery, while the trailing frontal band and associated rain is apparent throughout the series. The series shows the development of the second system and the resulting growth of the rain area.

D. COMPARISON WITH OTHER STUDIES

Many studies have been conducted to estimate rain area and rate with satellite imagery. Table X shows a comparison of several of these studies (including the analyses of this thesis) and their resulting success statistics. Techniques varied widely, and rain estimation was computed using VIS, IR, and combined VIS/IR imagery. The location of the regions analyzed is important, as the dynamics and resulting precipitation patterns vary greatly between midlatitude and subtropical systems.

Table X COMPARISON WITH VARIOUS RAIN ESTIMATION SCHEMES

Author										
	Lovejoy & Austin (1979)	Tsonis & Isaac (1985)	Negri & Adler (1987b)	Tsonis (1988)	O'Sullivan et al. (1990)	Frailey (1991)	Frailey (1991)			
Technique	Pattern Recog.	Cluster	Threshold	Threshold	Discrim. Analysis	Discrim. Analysis	Threshold			
Region	Montreal & GATE	Ontario, Canada	Southern Florida	Ontario, Canada	Southeast US	NE Atl. (ERICA)	NE Atl. (ERICA)			
Image Size (10 ⁵ km ²)	1.0	1.0	0.6	1.0	21.0	27.6	27.6			
No. images examined	25	18	83	18	330	3	3			
Ground Truth	Radar	Radar	Radar	Radar	Surface Reports	SSM/I	SSM/I			
Spectrum VIS/IR/Both	Both	Both	VIS IR	VIS IR	Both	IR Dev	IR Val			
POD	.55	.66	.98 .88	.62 .60	.81	.68 .62	.64			
FAR	--	.37	.13 .07	.38 .40	--	.21 .33	.40			
ERR	.13	.20	--- ---	.22 .30	.20	.30 .37	.38			

The first four studies listed in Table X each examined 18 to 83 images. Image area size was approximately $1 \times 10^5 \text{ km}^2$, due to the limitations involved using radar as ground truth. The O'Sullivan group used 30 days of hourly surface data as ground truth, which enabled analysis of 330 images of an area covering most of the Southeast US. For the studies in this thesis, only three images were studied. However, the extensive ground truth coverage yielded by the SSM/I swaths allowed analyses of images with areas larger than any those of previous studies. Thus, when comparing total image area analyzed, the two SSM/I studies in this thesis rank second behind O'Sullivan et al., and are nearly 30 times the area analyzed by the previous four studies. Additionally, the SSM/I swaths allows analysis of a broad range of latitude and consequent storm dynamics.

Table X shows that rain area delineation can be achieved with reasonably similar statistical results by a variety of VIS and IR schemes, including the methods used in this thesis. The work of Negri and Adler (1987b) and Tsonis (1988) is most comparable to the analyses presented in this study, in that thresholding using the IR spectral band was used. Negri and Adler's method gave, by the far, the best POD and FAR scores of all the schemes presented, but ERR scores were not computed. Considering location, Tsonis' work in Canada most nearly corresponds to the NE Atlantic area considered here. Tsonis' method yielded results quite similar to those obtained in this study. One important difference is that Tsonis' IR threshold was 245 K, where this study found

thresholds between 229 and 232 K. Additionally, Tsonis examined over-land areas using radar as ground truth, where this study examined oceanic areas using SSM/I as ground truth.

Comparison of this study's discriminant analysis and optimal thresholding results with those from a variety of other studies indicates that oceanic rain delineation success can be achieved with IR schemes, using SSM/I imagery as ground truth. This is significant, in that by calibrating GOES and SSM/I imagery to find an optimal IR rain threshold and updating that threshold as SSM/I imagery becomes available, large scale, continuous oceanic rain analyses can be completed.

VII. CONCLUSIONS AND RECOMMENDATIONS

Accurate global precipitation information is required by a wide variety of disciplines, including military applications. The development of satellite techniques, particularly rainfall algorithms using the microwave spectrum, has addressed this need. But the paucity of microwave data limits its usefulness for continuous rainfall coverage. The purpose of this study was to use hourly GOES IR satellite imagery to delineate oceanic rain/no-rain areas for three ERICA storms, using 12 h DMSP SSM/I rainrate analyses as ground truth.

After applying an exponential rainrate algorithm to the SSM/I data, both SSM/I and IR imagery were remapped to allow pixel-by-pixel intercomparison. Initial study of "cloud box" IR values and distribution histograms suggested that rain/no-rain areas could be delineated using IR mean, standard deviation and kurtosis. In general, rain areas exhibited colder IR mean cloud top temperatures and larger standard deviation. The distribution curves for cirrus areas, as described by standard deviation and kurtosis, appeared more Gaussian than those for rain areas.

The three variables IR mean, standard deviation and kurtosis were incorporated into a linear discriminant analysis scheme. The technique separated rain from no/rain areas within a mid/high cloud region, resulting in an average POD of 0.68 and ERR rate of 0.30 for development data (0.60 and 0.37 for validation data). Variations of the analysis revealed that IR mean played the dominant role in rain discrimination. Further

separation into rain intensity categories had very limited success, suggesting that IR data alone does not contain sufficient information to discriminate beyond rain/no-rain categories.

A simpler technique was applied to delineate rain areas with a single IR threshold, determined by optimizing a set of evaluation statistics. By minimizing percent misclassification and rain area size errors while maintaining sufficient POD, optimal IR thresholds were obtained for the ERICA storms analyzed. Thresholds ranged from 229 to 232 K and yielded an average POD of 0.64 and ERR of 0.38. Results were similar to those obtained by the discriminant analysis approach and schemes by various other authors.

Several recommendations are made for further development and operational implementation of these rain delineation techniques. This study assumed no prior probability and equal misclassification costs in order to allow comparison to other methods. However, an operational user is likely to have prior information on the likelihood of precipitation, as well as varying costs associated with over- or under-prediction of rain. These factors should be included in the development of the discriminant function or, if thresholding is used, in the weighting of terms in the CSI computation. This tailoring should improve the POD and ERR scores, and create a scheme better suited to the specific user.

Comparison with other studies shows that the choice of IR threshold is dependent on the location and dynamics of the storm system, and should be defined for each storm.

Evaluation of the techniques discussed here over various oceanic areas, latitude bands, and storm types may reveal generalized thresholds to use as starting points for analysis. This study restricted analysis to areas containing mid/high clouds, as defined by a 253 K screening threshold. While little SSM/I rain was associated with warmer clouds for the cases studied, the situation will differ for various locations and storms. It is critical that the screening threshold used be warm enough to include all precipitation events associated with the particular analysis area.

The main factor complicating the schemes used was the limited skill of IR in eliminating areas of cold cirrus clouds. This situation could be improved by inclusion of additional satellite data channels into the scheme. VIS data may be the simplest to incorporate, but is limited to daylight hours. Neu (1990) successfully identified cirrus with a split-window scheme, where a high brightness temperature difference (BTD) between AVHRR Channels 4 and 5 was attributed to the ice crystal emissivity and water vapor content of cirrus clouds. Any additional data to be included must be coincident in space and time, and would require image rectification.

Oceanic precipitation delineation is of significant importance to naval operations. Aviation interests and ship-based weapon systems operations are critically served by the knowledge of rain area location and intensity. A refined operational version of either precipitation delineation scheme presented here could be incorporated into the latest version of the Navy's Tactical Environmental Support System (TESS(3)) (Phegley and Crosiar 1991). Because of the differences in satellite platforms and scan modes, both

modes, both thresholding and discriminant analysis schemes require initial remapping of SSM/I and IR imagery. While thresholding is inherently a simpler operation, the repetitive computations required for each potential threshold increase its run time. Discriminant analysis requires more initial data preparation, but the discriminant functions themselves can be quickly obtained using the statistical packages available with TESS(3). Thus, both methods are competitive with respect to computational efficiency and results. The utilization of SSM/I imagery to determine rain area delineation functions or thresholds for GOES IR imagery can significantly enhance the acquisition of continuous, real-time global precipitation data.

APPENDIX A. STATISTICAL PARAMETERS

The statistical parameters used in this study are based on the work of Donaldson et al. (1975), Lovejoy and Austin (1979), and Tsonis and Isaac (1987). These parameters have become the unofficial standards for use in prediction of rain and various other meteorological phenomena. The parameters incorporate the use of four categories defined by the precipitation contingency table, Table XI (listed previously in Chapter VI as Table VII).

Table XI PRECIPITATION CONTINGENCY TABLE (after Lovejoy and Austin 1976)

		IR Prediction	
		Rain	No Rain
SSM/I Classification	Rain	HIT	MISS
	No Rain	FALSE ALARM	DRY

Two rain area definitions are made:

1. GOES RAIN = HIT + FALSE ALARM
2. SSMI RAIN = HIT + MISS

From these definitions, the statistical parameters used in this study are:

1. Probability of Detection (POD):

$$POD = \frac{HIT}{SSMI\ RAIN}$$

2. False Alarm Ratio (FAR):

$$FAR = \frac{FALSE\ ALARM}{GOES\ RAIN}$$

3. Critical Success Index (CSI):

$$CSI = \frac{HIT}{HIT + MISS + FALSE\ ALARM}$$

4. Percent Error (ERR):

$$ERR = \frac{MISS + FALSE\ ALARM}{HIT + MISS + FALSE\ ALARM + DRY}$$

5. Areal Error (AREA):

$$AREA = \frac{SSMI\ RAIN - GOES\ RAIN}{SSMI\ RAIN}$$

APPENDIX B. APPLIED OPTIMAL IR THRESHOLD

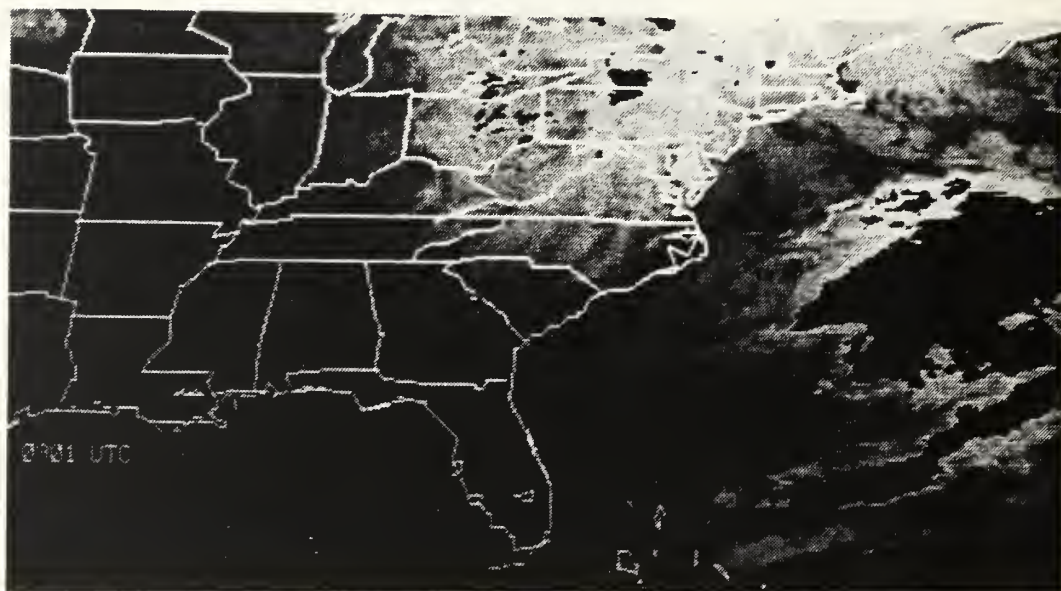


Fig. 16 GOES IR imagery for 13/0901 December 1988. Black area represents precipitation as determined by optimal IR threshold of 232 K.

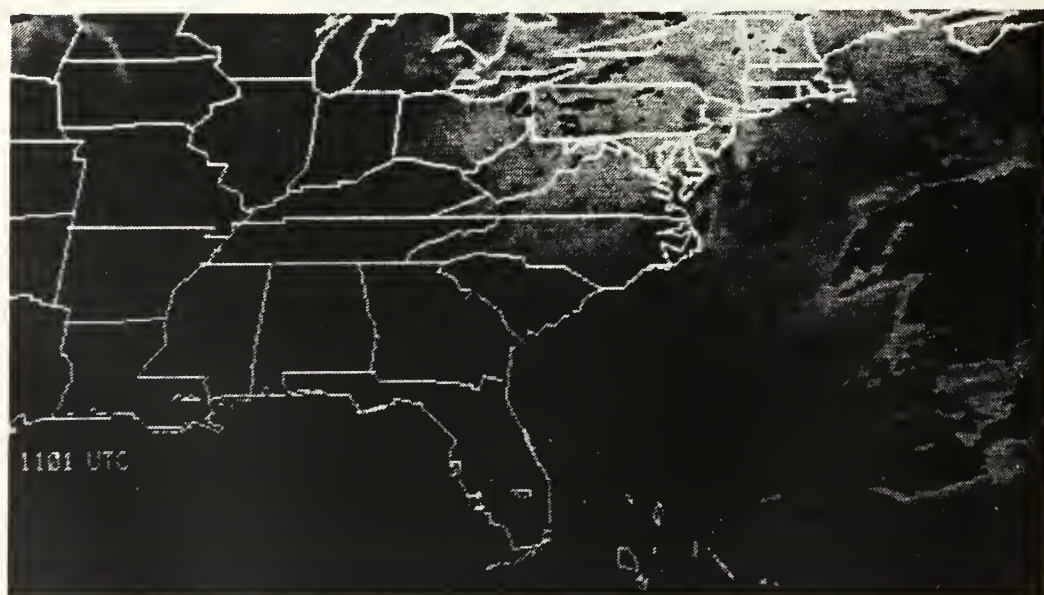


Fig. 17 As in Fig. 16, except 13/1101 December 1988.

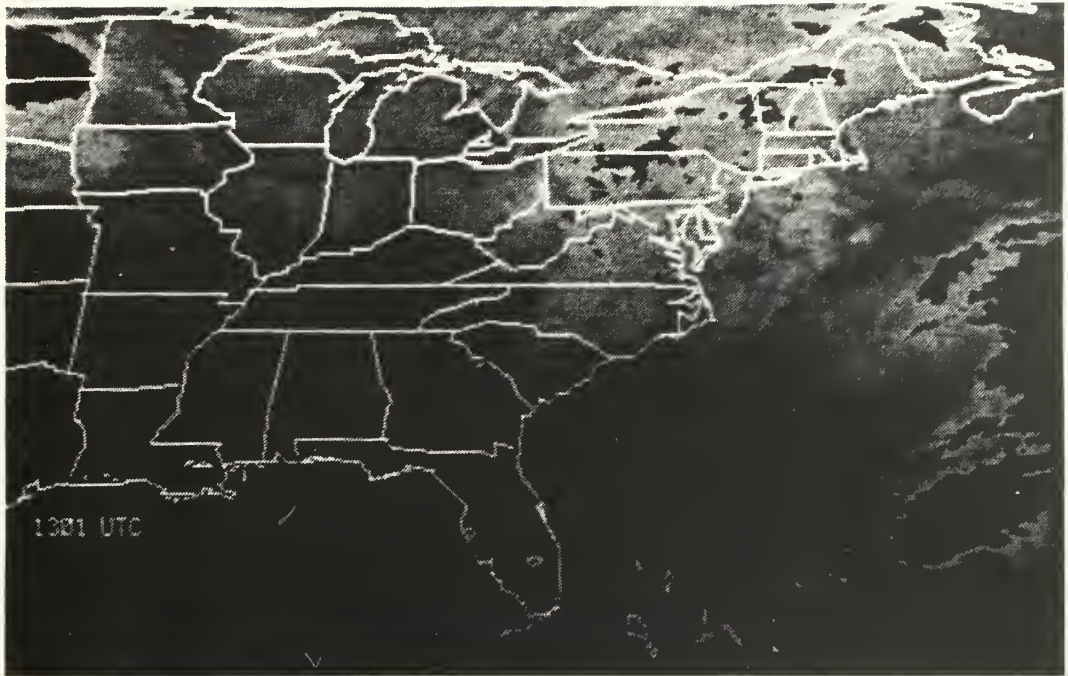


Fig. 18 As in Fig. 16, except 13/1301 December 1988.

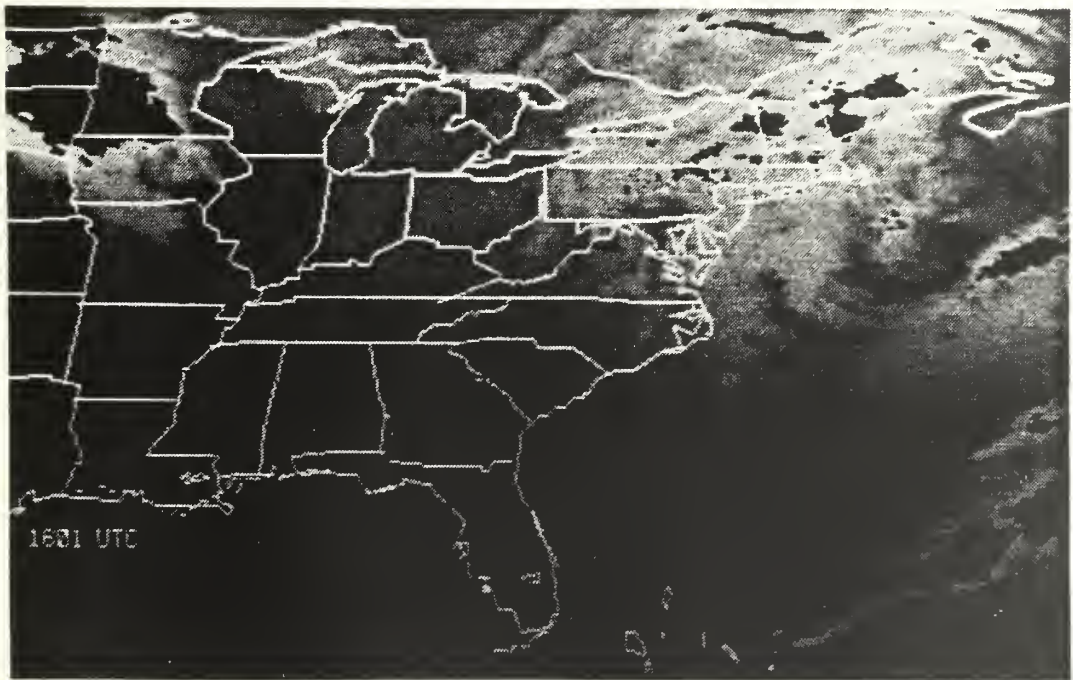


Fig. 19 As in Fig. 16, except 13/1601 December 1988.

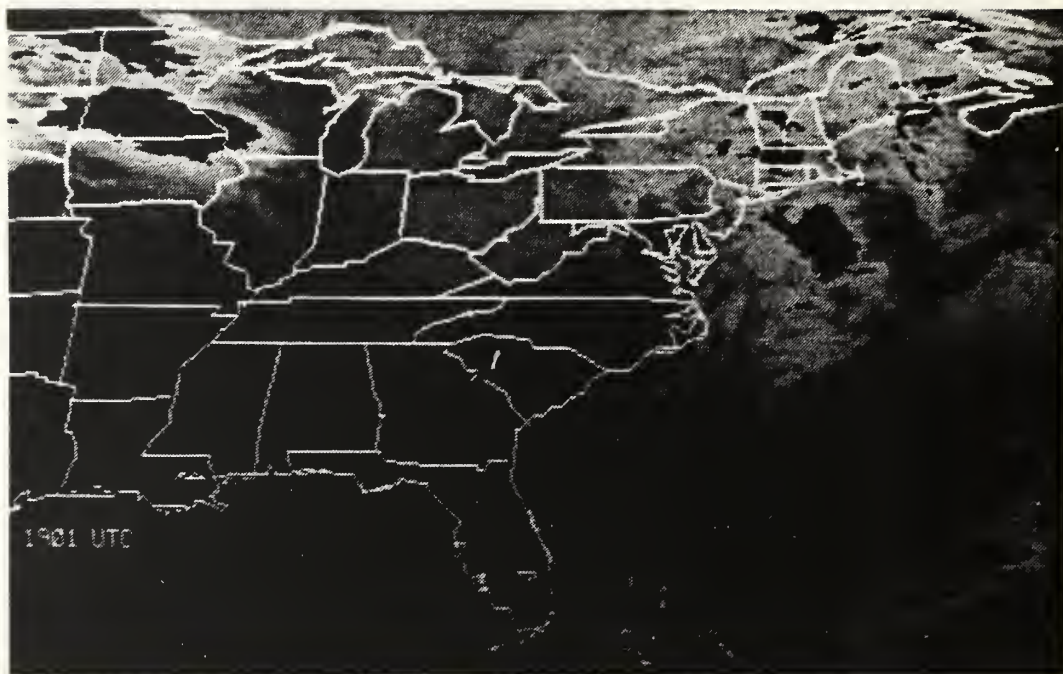


Fig. 20 As in Fig. 16, except 13/1901 December 1988.



Fig. 21 As in Fig. 16, except 13/2101 December 1988.

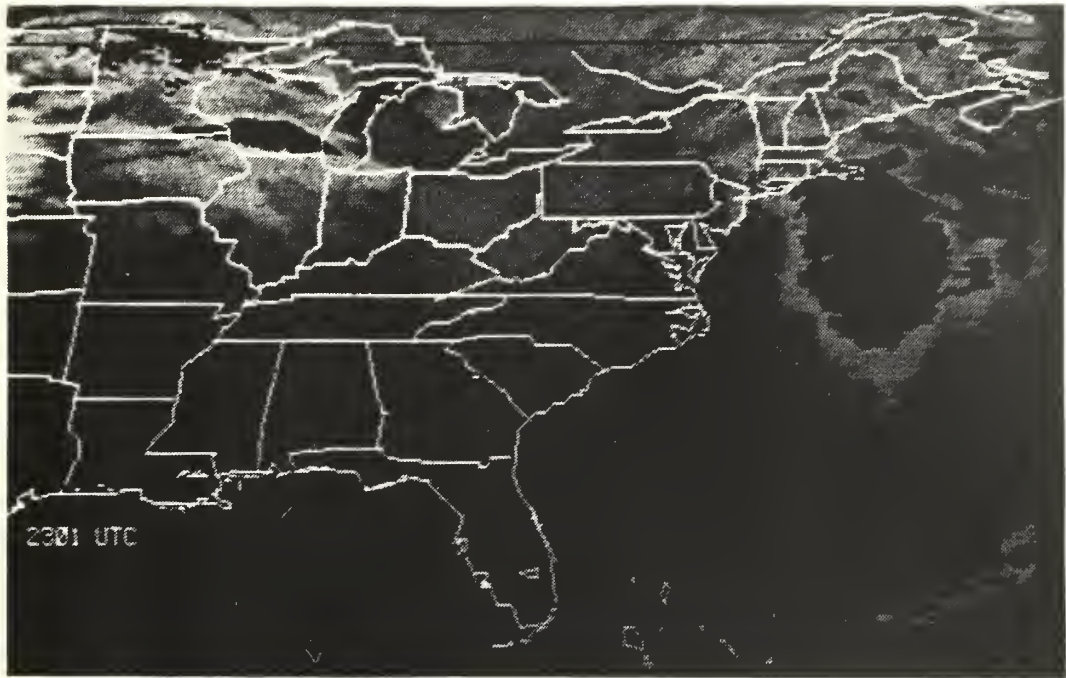


Fig. 22 As in Fig. 16, except 13/2301 December 1988.

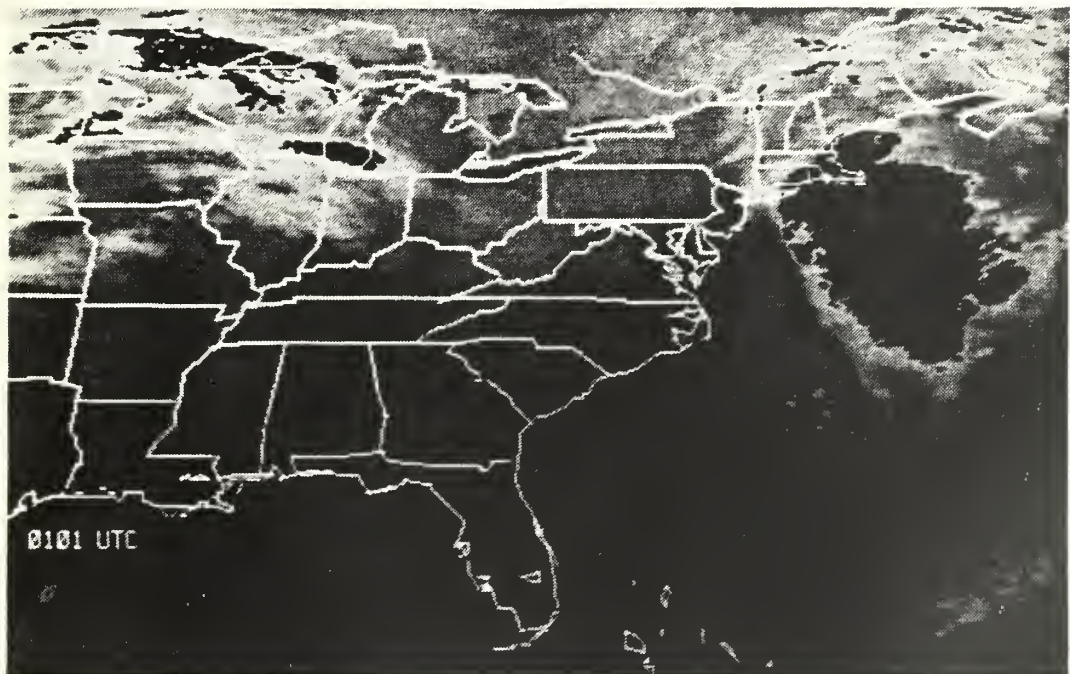


Fig. 23 As in Fig. 16, except 14/0101 December 1988.

LIST OF REFERENCES

- Adler, R. and A. Negri, 1988: A satellite infrared technique to estimate tropical convective and stratiform rainfall. *J. Appl. Meteor.*, **27**, 30-51.
- Almario, B.J., 1991: Precipitation analyses using SSM/I measurements for selected ERICA cyclones. M.S. Thesis, Naval Postgraduate School, Monterey, 68 pp.
- Barrett, E.C., and D.W. Martin, 1981: *The Use of Satellite Data in Rainfall Monitoring*. Academic Press, New York, 340 pp.
- Bellon, A., S. Lovejoy and G.L. Austin, 1980: Combining satellite and radar data for the short-range forecasting of precipitation. *Mon. Wea. Rev.*, **108**, 1554-1556.
- Bernstein, R., 1983: Image Geometry and Rectification, in *Manual of Remote Sensing Vol.I.*, R.N. Colwell, ed. American Society of Photogrammetry, Falls Church VA, 873-922.
- Brown, R., and M. Cheng, 1990: Investigation of techniques to delineate instantaneous precipitation areas using METEOSAT data. Preprints, Fifth Conf. on Satellite Meteorology and Oceanography, London, Amer. Meteor. Soc., 292-296.
- Burkland, G., and B.K. Ray, 1990: GRAFSTAT Primer. *IBM Research*, Yorktown Heights, NY, 98 pp.
- Cataldo, E., 1990: Evaluation of SSM/I rain analysis for selective storms in the ERICA project. M.S. Thesis, Naval Postgraduate School, Monterey, CA, 83 pp.
- Donaldson, R.J., R.M. Dyer and M.J. Kraus, 1975: An objective evaluator of techniques for predicting severe weather events. Preprints, Ninth Conf. on Severe Local Storms, Norman, Amer. Meteor. Soc., 321-326.
- Ensor, G.J. 1978: User's guide to the operation of the NOAA geostationary satellite system. National Environmental Satellite Service NOAA, U.S. Department of Commerce, Washington, D.C., October, 101 pp.

- Fisher, R.A., 1936: The use of multiple measurements in taxonomic problems. *Annals of Eugenics*, **7**, 179-188.
- Griffith, C.G., W.L. Woodley, P.G. Grube, D.W. Martin, J. Stout and D.N. Sikdar, 1978: Rain estimation from geosynchronous satellite imagery: Visible and infrared studies. *Mon. Wea. Rev.*, **106**, 1153-1171.
- Hadlock, R., and C.W. Kreitzberg, 1988: The experiment on rapidly intensifying cyclones over the Atlantic (ERICA) field study: objectives and plans. *Bull. Amer. Meteor. Soc.*, **69**, 1309-1326.
- Hartnett, E., G. Forbes and R. Hadlock, 1989: Experiment on Rapid Intensification of Cyclones over the Atlantic (ERICA) Field Phase Summary. Department of Physics and Atmospheric Science, Drexel University, Philadelphia, PA, 300 pp.
- Kidder, S.Q., and T.H. Vonder Haar, 1991: Principles of Satellite Meteorology. *Academic Press*, New York, in printing.
- King, P., 1990: On the relationship between GOES VIS and IR and radar rain rate. Preprints, Fifth Conf. on Satellite Meteorology and Oceanography, London, Amer. Meteor. Soc., 150-155.
- Lovejoy, S., and G.L. Austin, 1979a: The delineation of rain areas from vis and IR satellite data for GATE and mid-latitudes. *Atmos-Ocean*, **17**, 77-92.
- , and -----, 1979b: The sources of error in rain estimating schemes for GOES vis and IR satellite data. *Mon. Wea. Rev.*, **107**, 1047-1054.
- Negri, A. and R. Adler, 1987a: Infrared and visible satellite rain estimation. Part I: a grid cell approach. *J. Climate Appl. Meteor.*, **26**, 1553-1564.
- , and -----, 1987b: Infrared and visible satellite rain estimation. Part II: a cloud definition approach. *J. Climate Appl. Meteor.*, **26**, 1565-1576.
- Neu, T., 1990: Evaluation of generalized thresholds in an objective multispectral satellite cloud analysis. M.S. Thesis, Naval Postgraduate School, Monterey, CA, 50 pp.
- Olson, W.S., F.J. LaFontaine, W.L. Smith, R.T. Merrill, B.A. Roth, and T.H. Achtor, 1991: Precipitation Validation, in DMSP SSM/I Calibration/Validation Final Report, Vol.II. Naval Research Laboratory, Washington, D.C., 11-1 - 11-40.

- O'Sullivan, F., C.H. Wash, M. Stewart, and C.E. Motell, 1990: Rain estimation from infrared and visible GOES satellite data. *J. Appl. Meteor.*, **29**, 209-223.
- Phegley, L. and C. Crosiar, 1991: The third phase of TESS. *Bull. Amer. Meteor. Soc.*, **72**, 954-960.
- Rao, P.K., 1990: *Weather Satellites: Systems, Data and Environmental Applications*, American Meteorological Society, Boston, 503 pp.
- Reynolds, D.W., and T.H. Vonder Haar, 1976: A bispectral method for cloud parameter determination. *Mon. Wea. Rev.*, **105**, 446-457.
- Spencer, R.W., H.M. Goodman, and R.E. Hood, 1989: Precipitation retrieval over land and ocean with the SSM/I: Identification and characteristics of the scattering signal. *J. Atmos. Ocean Tech.*, **6**, 254-273.
- Stout, J.E., D.W. Martin and D.N. Sikdar, 1978: Estimating GATE rainfall with geosynchronous satellite images. *Mon. Wea. Rev.*, **107**, 585-598.
- Tsonis, A.A. and G.A. Isaac, 1985: On a new approach for instantaneous rain area delineation in the midlatitudes using GOES data. *J. Climate Appl. Meteor.*, **24**, 1208-1218.
- , 1988: Single thresholding and rain area delineation from satellite imagery. *J. Climate Appl. Meteor.*, **27**, 1302-1306.
- Wilheit, T.T., and A.T.C. Chang, 1980: An algorithm for retrieval of ocean surface and atmospheric parameters from the observations of the scanning multichannel microwave radiometer (SMMR), *Radio Science*, **15**, 525-544.

INITIAL DISTRIBUTION LIST

- | | | |
|----|--|---|
| 1. | Defense Technical Information Center
Cameron Station
Alexandria, VA 22304-6145 | 2 |
| 2. | Library, Code 52
Naval Postgraduate School
Monterey, CA 93943-5000 | 2 |
| 3. | Chairman (Code OC/Co)
Department of Oceanography
Naval Postgraduate School
Monterey, CA 93943-5000 | 1 |
| 4. | Chairman (Code MR/Hy)
Department of Meteorology
Naval Postgraduate School
Monterey, CA 93943-5000 | 1 |
| 5. | Professor Carlyle H. Wash (Code MR/Wx)
Department of Meteorology
Naval Postgraduate School
Monterey, CA 93943-5000 | 1 |
| 6. | Professor Philip A. Durkee (Code MR/De)
Department of Meteorology
Naval Postgraduate School
Monterey, CA 93943-5000 | 1 |
| 7. | LT Lisa E. Frailey, USN
Fleet Numerical Oceanography Center
Monterey, CA 93943-5005 | 1 |
| 8. | Commander
Naval Oceanography Command
Stennis Space Center
MS 39529-5000 | 1 |

- | | | |
|-----|---|---|
| 9. | Commanding Officer
Naval Oceanographic Office
Stennis Space Center
MS 39529-5001 | 1 |
| 10. | Commanding Officer
Fleet Numerical Oceanography Center
Monterey, CA 93943-5005 | 1 |
| 11. | Commanding Officer
Naval Oceanographic and Atmospheric
Research Laboratory
Stennis Space Center
MS 39529-5004 | 1 |
| 12. | Director
Naval Oceanographic and Atmospheric
Research Laboratory
Monterey, CA 93943-5006 | 1 |
| 13. | Chief of Naval Research
800 N. Quincy Street
Arlington, VA 22217 | 1 |

Thesis

F683 Frailey

c.1 Integrated microwave and
infrared precipitation
analysis.

Thesis

F683 Frailey

c.1 Integrated microwave and
infrared precipitation
analysis.



3 2768 00034120 0